

Simulation of a sea ice ecosystem using a hybrid model for slush layer desalination

Benjamin T. Saenz¹ and Kevin R. Arrigo¹

Received 23 August 2011; revised 2 January 2012; accepted 5 January 2012; published 4 May 2012.

[1] Porous, slushy layers are a common feature of Antarctic sea ice and are often colonized by high concentrations of algae. Despite its potential importance to the physics and biogeochemistry of the sea ice ecosystem, current knowledge of the evolution of sea ice slush layers is limited. Here we present a model of sea ice that is capable of reproducing the vertical biophysical evolution of sea ice that contains slush layers. The model uses a novel hybrid desalination scheme to calculate salt fluxes and brine motion during freezing using one of two different methods depending on the brine fraction of the ice. Model runs using atmospheric and snow depth forcing from the Ice Station Weddell experiment show that model is able to simulate the magnitude and timing of sea ice temperature, salinity, and associated algal growth of observed slush layers, as well as the surrounding sea ice. The model was designed with regional-scale simulations in mind and we show that the model performs well at lower vertical resolutions, as long as the slush layer is resolved. Incorporation of our model of slush ice desalination into regional and global simulations has potential to improve model estimates of salt, heat, and biochemical fluxes in polar marine environments.

Citation: Saenz, B. T., and K. R. Arrigo (2012), Simulation of a sea ice ecosystem using a hybrid model for slush layer desalination, *J. Geophys. Res.*, 117, C05007, doi:10.1029/2011JC007544.

1. Introduction

[2] Porous, slushy layers within sea ice are a significant feature across much of the Antarctic ice pack. Composed of a mixture of brine and ice crystals of varying sizes, slush layers contain a high proportion of fluid relative to typical sea ice, often 50% or greater [Fritsen *et al.*, 2001]. These layers can arise via flooding of snow at the snow/ice interface due to high snow loading or ridging and rafting of ice floes, or via melting of near-surface sea ice due to inverted summertime temperature gradients and other processes ('gap layers' [Ackley *et al.*, 2008]).

[3] Slush layers play a significant physical and ecological role in the Southern Ocean. The freezing of slush layers can result in the rejection of a significant amount of salt into the water column below [Lytle and Ackley, 1996]. High concentrations of sea ice algae are typical of slush layers, which are often stained brown with algal pigments [Ackley and Sullivan, 1994; Fritsen *et al.*, 1994; Kattner *et al.*, 2004]. Primary production by sea ice algae in flooded layers is thought to constitute a large fraction of the total carbon fixed in Antarctic pack ice [Arrigo *et al.*, 1997, 1998]. Establishing where and when slush layers form, as well as their fate, would further our understanding of carbon cycling in the

Antarctic and how it may change under altered environmental conditions.

[4] In-situ studies of sea ice are necessarily limited in space and time because of logistical difficulties associated with sampling in such a remote and hostile environment. Models of sea ice have therefore served as important tools for investigating sea ice dynamics and estimating algal production and carbon flux on large scales [Arrigo *et al.*, 1997]. Current models are relatively mature in their ability to simulate growth and advection of sea ice at a hemispheric scale [Hunke and Dukowicz, 1997; Holland *et al.*, 2008]; however, the processes of fluid transfer and phase change that define the evolution of sea ice salinity and associated brine fluxes are typically restricted to micro-scale investigations [Wetlaufer *et al.*, 1997; Schulze and Worster, 1999; Jackson and Cheadle, 1998; Maksym and Jeffries, 2001]. Simulations by Vancoppenolle *et al.* [2009] provide the first estimates of hemispheric sea ice salinity evolution, although the ability to simulate slush layer evolution was diminished by tracking a single bulk salinity tracer, and using standardized rather than dynamic salinity profiles.

[5] After a slush layer is formed via seawater flooding or melting of ice or snow, the brine in the slush layer can become relatively isolated. Exchange between the slush ice and the underlying seawater is facilitated by several different mechanisms, including wave and ice floe motion and surface depression due to ridging and rafting of ice floes or snow loading [Arrigo *et al.*, 2010]. The most notable cause of fluid flux with respect to primary production occurs during freezing of the slush layer, when brine density gradients that

¹Department of Environmental Earth System Science, Stanford University, Stanford, California, USA.

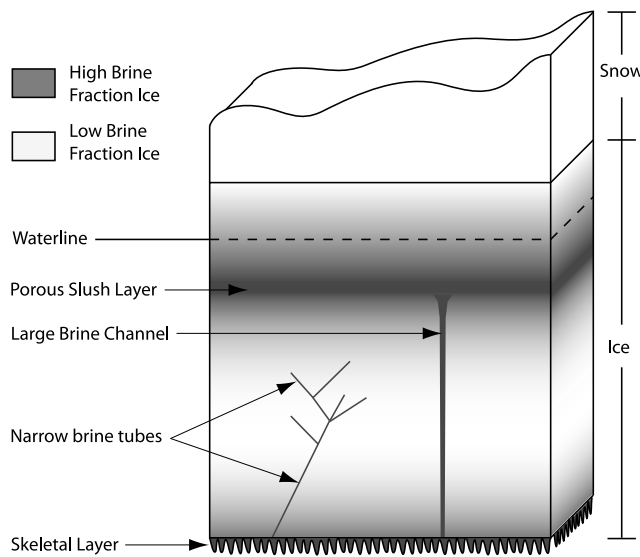


Figure 1. Cut-away section of sea ice showing sea ice internal structure and brine features that influence desalination. Here a porous slush layer (dark gray) below the waterline is connected to the ocean below via a large brine channel, facilitating rapid desalination. Below the slush layer, the sea ice is less saline with a lower brine fraction (light gray), and contains connected narrow brine tubes. In the desalination model, the slush layer and skeletal layer desalinate rapidly according to a stable salinity scheme, while the remaining low brine fraction sea ice desalinated more slowly according to the equations of *Cox and Weeks* [1988].

result in desalination can cause rapid overturning of brine [Fritsen *et al.*, 1994]. With the potential to replace brine in the slush layer multiple times during the course of freezing, slush layers possess the ability to replenish nutrients to growing sea ice algal communities.

[6] Recent modeling efforts have made large strides in representing desalination and fluid flux of sea ice via gravity drainage. Current studies indicate that the sea ice desalination and associated fluid flux is a continuous process promoted and limited simultaneously by both the ice growth rate and the ice geometry, and ideally should be modeled as a single process [Notz and Worster, 2009]. Research evaluating sea ice as a ‘mushy’ structure allows use of continuum equations that, in theory, permit mechanistically modeled desalination and associated fluid flow at any location in the ice, regardless of state. Convective desalination occurs when the Rayleigh number of the sea ice system reaches a critical value, with fluid flux determined by Darcy’s law [Worster, 1997; Wettlaufer *et al.*, 1997]. Maksym and Jeffries [2001] specifically addressed the issue of surface slush layer desalination using a micro-scale two-dimensional model that tracked heat, salt, and momentum, concluding that desalination was highly dependent on the permeability of the underlying sea ice. Using an approximate one-dimensional collapse of the mushy layer equations to a parameterized advection–diffusion equation, Vancoppenolle *et al.* [2010]

obtain reasonable sea ice salinity profiles, thereby generating a mechanistically derived fluid flux.

[7] However, several factors contribute to a potentially high level of uncertainty in such simulations, especially when considering slushy ice. These equations depend on a workable permeability parameterization for sea ice, and such a parameterization remains elusive for high-brine volume sea ice due to the geometric complexity of the ice interior (Figure 1). Permeability-porosity relationships have been measured [Freitag, 1999; Eicken *et al.*, 2002; Freitag and Eicken, 2003] and modeled [Golden *et al.*, 2007] with some success at low brine fractions; however, the majority of brine is rejected at higher brine fractions, and these parameterizations do not capture the fluid dynamics of the warm, porous interior layers where algae thrive. Variations in measured permeability of up to an order of magnitude at a particular brine fraction point out the extreme heterogeneity of the sea ice environment. Furthermore, at high brine fractions with complex brine tube geometries, Darcy’s law may not be an appropriate predictor of fluid velocity, calling into question the calculations of fluid flux across a relatively thick slush layer using mushy layer equations that do not incorporate a faster type of fluid transfer. When combined, the above factors produce an uncertainty in the calculation of brine flux that currently is difficult to estimate due to the paucity of brine flux measurements. Finally, these problems are compounded when large-scale models must integrate naturally heterogeneous sea ice properties across grid sizes spanning hundreds of square kilometers. Given then the low resolution of global scale simulations, a simpler empirical calculation may suffice to estimate slush layer desalination and associated brine fluxes.

[8] Here we present a coupled biological-physical model of sea ice appropriate for large-scale estimation of slush layer dynamics. The model is developed from time series observations of sea ice and relies on previously published methods for simulation of cold, low-salinity sea ice [Eicken, 1992; Bitz and Lipscomb, 1999; Maksym and Jeffries, 2000; Kottmeier *et al.*, 2003] and algal growth and physiology [Arrigo and Sullivan, 1994]. To simulate slush layer physics, we introduce a quasi-empirical parameterization of convective desalination and brine exchange that is based upon established sea ice dynamics and the estimation of a ‘stable salinity’ after rapid desalination during initial sea ice formation [Nakawo and Sinha, 1981; Cox and Weeks, 1988; Petrich *et al.*, 2006].

[9] Without actual measurements of brine flux, researchers must calibrate models to proxies for the actual desalination process, such as the evolution of temperature and bulk salinity profiles and the changes in dissolved tracer concentrations within the brine. Our model is developed and tested using constraints of sea ice salinity, temperature, fluid flux, and sea ice algal growth from time series observations of these properties measured *in situ* in 1992 at Ice Station Weddell (ISW) Site B [Fritsen *et al.*, 1994; Ackley *et al.*, 1996; Lytle and Ackley, 1996]. This study site contained a thick slush layer that froze during the course of observations. We further assess the robustness of the model by simulating ISW Site A, which contained a similar slush layer but with different, and more heterogeneous, ice and snow conditions. We discuss physicality of our desalination and heat transfer

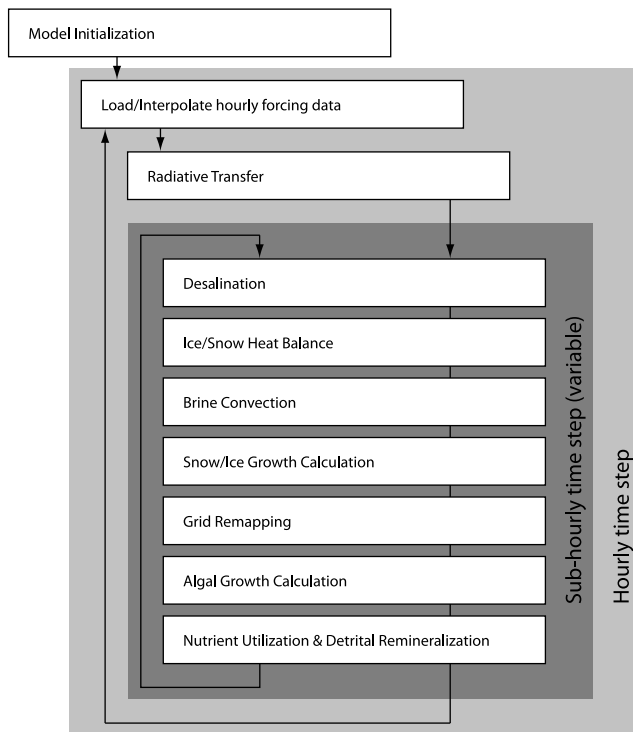


Figure 2. Model conceptual schematic showing the major components of the sea ice model in the order that they occur. Forcing data interpolation and radiative transfer are calculated using a 1-hour time step. The remaining physical, biological, and gridding processes use a smaller time step that is determined at run time to reduce numerical errors. Desalination and associated convective heat flux is calculated first, so it can be included in the following heat transfer calculation.

parameterizations, limitations and applicability of the model, and possibilities for further refinement.

2. Model Description

[10] Here we describe the logical components and computational flow of the sea ice ecosystem model, with justification of important parameterizations. The operations executed at each model time step are shown in Figure 2. Mathematical symbol notation and numerical constants can be found in Tables 1 and 2, respectively.

2.1. Model Grid

[11] Ice and snow are represented by a variable number of discrete horizontal layers. The physical ice state and macronutrient, microalgae, and detritus concentrations are tracked in each layer. In the snow and ice interior, these layers are nominally 0.01 m thick, although they may grow slightly larger to accommodate the exact ice height. Changes in ice or snow thickness are accounted for by growing and shrinking all layers, followed by conservative remapping of mass, heat and tracers to the new layers. Once the total ice thickness has changed by 0.01 m, a layer is added or subtracted, and the ice or snow thickness is divided equally among the new number of layers. This layering scheme allows the layer thicknesses to remain approximately constant while still resolving arbitrary thickness changes, and

Table 1. Symbol Notation

	Definition
T	Ice or snow temperature ($^{\circ}\text{C}$, Kelvin)
S	Salinity of ice or brine (psu)
ϕ	Brine or ice fraction (fraction)
C	Solute concentration (mg m^{-3})
V	Fluid volume ($\text{m}^3 \text{m}^{-2}$)
F	Energy flux (W m^{-2})
c	Specific heat capacity of ice or snow ($\text{J g}^{-1} \text{K}^{-1}$)
k	Thermal conductivity of ice or snow ($\text{W m}^{-1} \text{K}^{-1}$)
z	Vertical axis distance (m)
h	Ice or snow thickness (m)
ρ	Density bulk ice, pure ice, brine, or snow (g m^{-3})
r	Stoichiometric ratio (mol mol^{-1} , g g^{-1})
q	Volumetric heat (J m^{-3})
R	Rate constant (s^{-1} , day^{-1})

minimizes remapping errors at the boundaries. The vertical resolution may be changed by specifying a different nominal layer thickness (see section 3.4.4).

[12] The model grid also incorporates a discrete skeletal region at the ice/water interface that is fixed at the seawater temperature and has a 50% brine fraction [Arrigo *et al.*, 1993]. The maximum skeletal layer thickness is 0.02 m after Arrigo and Sullivan [1994] and Fritsen *et al.* [1998]. The skeletal layer is represented by two horizontal layers that can vary in thickness from 0.001–0.01 m. During sea ice growth, the skeletal layers grow before the internal ice layers, up to the maximum specified skeletal layer thickness.

Table 2. Model Parameters and Constants

Parameter	Description	Value	Units
G_0	Maximum algal growth rate at 0°C	0.81	day^{-1}
R_g	Algal temperature-dependant growth rate constant	0.631	$^{\circ}\text{C}^{-1}$
R_m	POC remineralization rate	0.03	day^{-1}
f_e	Remineralization efficiency	1	fraction
$E'_{k_{\max}}$	Maximum spectral photoadaptation parameter	18	$\mu\text{Ein m}^{-2} \text{s}^{-1}$
A	Spectral photoadaptation equation constant	1.4	dimensionless
B	Spectral photoadaptation equation constant	0.12	dimensionless
$r_{C:Chla}$	Algal/detritus C:Chla ratio	35	g/g
$r_{C:N}$	Algal/detritus C:N ratio	7	mol/mol
$r_{C:P}$	Algal/detritus C:P ratio	106	mol/mol
$r_{C:Si}$	Algal/detritus C:Si ratio	4	mol/mol
K_{NO3}	Half-saturation algal rate constant for NO_3 uptake	1	μM
K_{NH4}	Half-saturation algal rate constant for NH_4 uptake	1	μM
K_{PO4}	Half-saturation algal rate constant for PO_4 uptake	0.1	μM
K_{SiOH4}	Half-saturation algal rate constant for SiOH_4 uptake	60	μM
C_{sw_NO3}	Seawater NO_3 concentration	30	μM
C_{sw_NH4}	Seawater NH_4 concentration	0	μM
C_{sw_PO4}	Seawater PO_4 concentration	2	μM
C_{sw_SiOH4}	Seawater SiOH_4 concentration	80	μM
C_{sw_POC}	Seawater detritus concentration	0	$\mu\text{g L}^{-1}$
μ	Liquidus slope of water	0.054	dimensionless
c_{i0}	Specific heat of pure ice	2.011	$\text{J g}^{-1} \text{K}^{-1}$
c_w	Specific heat of seawater at 0°C	3.96	$\text{J g}^{-1} \text{K}^{-1}$
L	Latent heat of fusion of water	334	J g^{-1}
κ_{NIR}	Spectrally-weighted near-IR absorption coefficient	7.18	m^{-1}

After the skeletal layer has reached maximum thickness, further ice growth results in the transfer of ice and tracers from the skeletal layers to the bottom interior ice layer as congelation ice. New ice and water column tracer values are then incorporated into the skeletal layer in equal proportion to those removed to maintain skeletal layer thickness. During conditions of ice melt, the skeletal layer melts before the congelation ice.

2.2. Thermodynamics

[13] The surface heat flux (F_0) at the boundary between the atmosphere and either the sea ice or overlying snow cover accounts for incoming longwave radiation (F_L), outgoing longwave radiation (F_I), turbulent latent heat (F_e), turbulent sensible heat (F_s), and conductive heat (F_c)

$$F_0 = F_L + F_I + F_e + F_s + F_c. \quad (1)$$

[14] Calculation of F_L , F_I , F_e , and F_s from measurements of atmospheric temperature, wind speed, humidity, and surface temperature follows *Kottmeier et al.* [2003]. F_c is the product of ice thermal conductivity (k) and the temperature gradient between the ice surface and uppermost ice layer ($\partial T/\partial z$). Where measured values for atmospheric variables were not available, we applied linearly-interpolated 6-hourly surface atmospheric data from the European Centre for Medium-Range Weather Forecasts (ECMWF) Interim reanalysis. The maximum snow or ice surface temperature is set to 0°C .

[15] Heat transfer within the snow and sea ice is accomplished using a modified form of the heat equation that accounts for internal heating by absorption of shortwave radiation (F_i – described in section 2.4)

$$\rho c \frac{\partial T}{\partial t} = \frac{\partial}{\partial z} k \frac{\partial T}{\partial z} + \frac{\partial}{\partial z} F_i \quad (2)$$

where ρ is the snow or ice layer density (g m^{-3}), c is the snow or ice specific heat capacity ($\text{J g}^{-1} \text{K}^{-1}$), T is the temperature ($^\circ\text{C}$), and z is the vertical inter-layer distance (m). The thermal conductivity (k) of sea ice ($\text{W m}^{-1} \text{K}^{-1}$) follows measurements of *Pringle et al.* [2007]

$$k = \frac{\rho}{\rho_i} \left(2.11 - 0.11T + 0.09 \frac{S}{T} - \frac{\rho - \rho_i}{1000} \right) \quad (3)$$

where ρ_i is the density of pure ice (918 kg m^{-3}) and S is the bulk sea ice salinity (psu), or the salinity of the resulting water should the ice be completely melted. For snow layers, we chose to fix k at $0.4 \text{ W m}^{-1} \text{K}^{-1}$. Although the k of snow is variable at different snow densities and grain sizes, owing to the complexity of snow metamorphosis, we choose to hold this parameter constant. The thermal conductivity used here is higher than the value of $0.33 \text{ W m}^{-1} \text{K}^{-1}$ derived experimentally by *Sturm et al.* [2002] and used in other sea ice growth in other models [*Ebert and Curry*, 1993; *Wu et al.*, 1999]. We choose to use a higher value since it was not possible to reproduce observed thermal profiles using $k = 0.33 \text{ W m}^{-1} \text{K}^{-1}$. A higher value for k may be justified due to the timing of observations, since ISW observations begin in late summer when higher values for

k are expected in dense, refrozen snow. The volume-based heat capacity (c , $\text{J g}^{-1} \text{K}^{-1}$) for sea ice is calculated as

$$c_i = 2.0113 + \frac{\mu SL_w}{T_0 T_1} \quad (4)$$

after *Bitz and Lipscomb* [1999], where T_0 and T_1 (K) are the old and new temperatures of the layer across a model time step, L_w is the latent heat of fusion of pure water (334 J g^{-1}), and $\mu = 0.054$ (dimensionless) is the slope of the linear liquidus (freezing temperature) relationship. Above the liquidus temperature ($T_m = -\mu S$), the heat capacity of the resultant liquid brine (c_b) is assumed to equal the heat capacity of seawater at 0°C , or $3.96 \text{ J g}^{-1} \text{K}^{-1}$. The heat capacity ($\text{J g}^{-1} \text{K}^{-1}$) of the snow (c_s) is assumed to be identical to that of pure ice [*Fukusako*, 1990]

$$c_s = 0.185 + 0.00689T. \quad (5)$$

[16] Heat flux across the bottom sea ice-water boundary is assumed to be purely conductive. The sum of the ocean heat flux (F_w , W m^{-2}) from below and the conductive heat flux (F_c , W m^{-2}) from above is balanced by the accretion and melting of ice at the boundary, such that

$$F_w + F_c = -q_b \frac{dh}{dt} \quad (6)$$

where dh/dt (m s^{-1}) is the change in ice thickness and q_b (J m^{-3}) is the salinity-dependent heat of fusion of sea ice determined by integration of the ice specific heat capacity c_i and multiplying by the layer density ρ (g m^{-3}):

$$q_b = 2.0113 \rho [(T_m - T) + L_w(1 - T_m/T)] \quad (7)$$

[*Bitz and Lipscomb*, 1999].

[17] The heat equation solutions for each layer are computed using an implicit space-centered 1st-order staggered-grid discretization [*Tannehill et al.*, 1997]. When combined with the top and bottom boundary fluxes, the ice and snow layer heat flux equations form a system of linear equations that, because of the dependence of c_i and c_s on T , is solved iteratively using Newton–Raphson stepping.

2.3. Sea Ice State

[18] By assuming that the two-phase system of ice and brine is in thermal equilibrium, we may derive pertinent sea ice parameters from the two state variables S and T [*Cox and Weeks*, 1988; *Arrigo et al.*, 1993]. For heat accounting due to grid remapping and ice accretion or melting, we calculate an ice reference enthalpy (q_i , J m^{-3}) relative to 0°C . The value for q_i is found similarly to q_b , with the addition of an extra term to account for the fully liquid phase

$$q_i = -2.0113 \rho_i [(T_m - T) + L_w(1 - T_m/T)] - \rho_{T_m} T_m c_w \quad (8)$$

where ρ_{T_m} (g m^{-3}) is the density of brine at the melting temperature T_m . Reference enthalpy (q_s) for snow (J m^{-3}) is found similarly by

$$q_s = \rho_s (-0.185T - 0.003445T^2). \quad (9)$$

Table 3. Intrinsic Optical Properties (IOPs) of Ice and Snow Classes Used by the Delta-Eddington Spectral Shortwave Attenuation Model^a

	Scattering Coefficient σ (m ⁻¹)	Asymmetry Parameter g	Absorption Coefficient κ (m ⁻¹)
New/cold snow	2500	0.89	$\phi_i \kappa_i(\lambda) + 0.3$
Warm/old snow	900	0.94	$\phi_i \kappa_i(\lambda) + 0.3$
Drained surface ice	900	0.94	$\phi_i \kappa_i(\lambda) + 0.3$
Sea ice (>-2)	$15 + \gamma(C_{chla} + C_{POC})$	0.98	$\phi_i \kappa_i(\lambda) + \phi_b \kappa_w(\lambda) + \kappa_{chla}(\lambda) (C_{chla} + C_{POC})$
Sea ice (-10 to -2°C)	$15 + 9.6S(\text{abs}(T)-2) + \gamma(C_{chla} + C_{POC})$	0.98	$\phi_i \kappa_i(\lambda) + \phi_b \kappa_w(\lambda) + \kappa_{chla}(\lambda) (C_{chla} + C_{POC})$
Sea ice (-22 to -10°C)	$15 + 76.8S + \gamma(C_{chla} + C_{POC})$	0.98	$\phi_i \kappa_i(\lambda) + \phi_b \kappa_w(\lambda) + \kappa_{chla}(\lambda) (C_{chla} + C_{POC})$
Eutectic sea ice (<-22°C)	$2400 + \gamma(C_{chla} + C_{POC})$	0.94	$\phi_i \kappa_i(\lambda) + \phi_b \kappa_w(\lambda) + \kappa_{chla}(\lambda) (C_{chla} + C_{POC})$

^aSea ice scattering coefficients incorporate algal scattering, represented by the combined algae and POC concentration in units of mg C m⁻³ times a scaling factor in units of m² mg⁻¹ (γ). Scaling factor $\gamma = 5.26 \times 10^{-3}$ for all model runs, and is calculated from the observation of scattering by large particles in seawater of 1×10^{-3} m²/mg dry mass [Babin *et al.*, 2003] times a dry mass/carbon conversion ratio of 5.26 g/g C for diatoms [Sicko-Goad *et al.*, 1984].

[19] After a change in enthalpy of an ice or snow layer under steady state conditions due to a change in the vertical grid size, new layer state temperatures are derived by solving equations (8) or (9) for T , thereby conserving total heat.

2.4. Solar Irradiance

[20] Because scattering, rather than absorption, dominates attenuation of solar irradiance in snow and sea ice, exponential decay, as represented by Beer's law, does not accurately simulate radiative transfer in the sea ice environment, especially when optically thin layers are present [Barber *et al.*, 1991; Jin *et al.*, 1994]. Since snow cover is thin over a large fraction of both the Arctic and Antarctic ice packs during spring when algae are growing, we incorporated a radiative transfer model that more accurately simulates thin-layer optical scattering.

[21] We chose a two-stream spectral radiative transfer model based on the delta-Eddington approximation for the scattering phase function that accounts for multiple scattering effects on direct and diffuse radiation [Briegleb and Light, 2007]. Levels of scattering in sea ice and snow show large variation with density, brine volume, ice grain size, and temperature [Warren, 1982; Light *et al.*, 2003]. The complexity of a continuous model of scattering, such as derived by Light *et al.* [2004], is too computationally intensive to be incorporated into our model. Therefore, we narrowed our scattering parameterizations to five classes of snow and sea ice that demonstrate very different optical properties: (1) cold snow, (2) warm snow, (3) warm sea ice, (4) cold mirabilite-containing sea ice, and (5) eutectic sea ice. For each class, the inherent optical properties (IOPs) of the snow or sea ice were specified using published absorption and scattering phase function values, followed by manual tuning of scattering coefficients until modeled spectral albedos and asymptotic extinction coefficients matched observed values from Warren and Wiscombe [1980] and Grenfell and Maykut [1977]. Resulting IOPs for each class of snow and ice fall within bounds for these parameters reported by Briegleb and Light [2007], Light *et al.* [2008], and Ehn *et al.* [2008], and are listed in Table 3.

[22] The delta-Eddington model calculates the spectral (upwelling and downwelling) irradiance and heat absorption in the photosynthetically available radiation (PAR) band, using 31 equal wavelength bins between 400 and 700 nm. Surface non-PAR shortwave solar radiation (350–400 nm and 700–4000 nm) is estimated as a constant fraction of total

PAR, and attenuated as a single band using a spectrally-weighted absorption coefficient. For the purposes of short-wave heating, we take the mean of heat absorption across the snow distribution for each band, and then the total heat absorption from all bands is incorporated into the heat flux (equation (2)) as F_i .

[23] Incident direct and diffuse surface atmospheric irradiance are calculated from the clear-sky radiative transfer model of Gregg and Carder [1990], and then corrected for clouds as by McClain *et al.* [1996]. Atmospheric parameters from the NCEP/NCAR Reanalysis 2, along with TOMS ozone concentrations, were used as input to the atmospheric radiative transfer model.

2.5. Biological Model

[24] The biological component of the model is modified from Arrigo and Sullivan [1994] and includes ice microalgae, grazing/death, and multiple nutrients, including NO₃, NH₄, PO₄, and Si(OH)₄. To this we added a detritus pool that consists of grazed/dead microalgae and convects with brine movement, while microalgae maintain their position within the ice sheet [Welch and Bergmann, 1989]. Nutrients are recycled from the detrital pool to NH₄ and PO₄ according to

$$C_N = f_e r_{N:C} C_{Det} e^{R_m t} \quad (10)$$

where C_N [M] is the nutrient concentration, C_{Det} [g C m⁻³] is the detrital concentration, f_e [dimensionless] is the fractional efficiency of remineralization, $r_{N:C}$ is a constant nutrient:carbon ratio [mol N g C⁻¹] and R_m [day⁻¹] is the specific remineralization rate (Table 2). Algae utilize NO₃ and NH₄ in proportion to their availability and maximum growth rates are calculated according to Bissinger *et al.* [2008].

[25] Sea ice algae are motile within the ice [Welch and Bergmann, 1989] so we allow them to move toward the bottom of the ice sheet according to a linear relationship with the ice growth rate [Lavoie *et al.*, 2005]. At rates of ice growth below 0.015 m day⁻¹, algae move downward according to the relationship:

$$\Delta h_a = 1 - \frac{dh/dt}{1.5} \quad (11)$$

where Δh_a (cm day⁻¹) is the vertical distance of algal migration during a model time step and dh/dt (cm day⁻¹) is

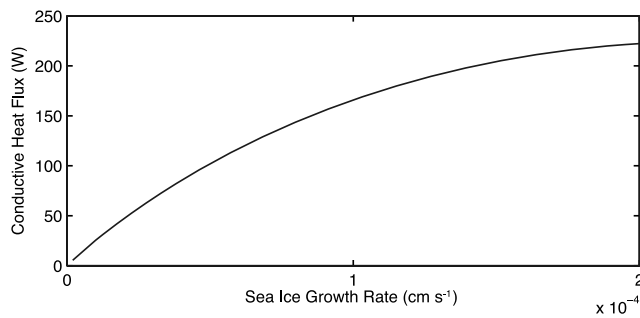


Figure 3. The relationship between heat flux and basal sea ice growth rate using an empirical stable salinity relationship [Petrich *et al.*, 2006] and sea ice state equations [Cox and Weeks, 1988] at a brine temperature of -1.8°C . A least squares regression of the relationship allows prediction of the ice growth rate from the heat flux (positive upward) and is used in the model to calculate the desalination rate in high brine fraction sea ice.

the ice growth rate. At ice growth rates higher than 0.015 m day^{-1} , we assume that algae become trapped within the advancing ice and are not able to move. Downward movement by ice algae can result in greater algal production by allowing an algal population to remain in a warmer, generally more nutrient-rich environment. In contrast to Lavoie *et al.* [2005], modeled algae cannot migrate upwards in the ice pack during periods of bottom ice melt.

2.6. Desalination

[26] Sea ice desalination has been previously divided into two classes, interface desalination (also termed brine rejection or skeletal desalination) near the ice-seawater interface, and interior desalination of the colder sea ice away from the ice-seawater interface [Cox and Weeks, 1975, 1988; Wettlaufer *et al.*, 1997]. Interface desalination is considered to be responsible for rapidly segregating the majority of salt from freezing seawater, until an empirically-observed ‘stable salinity’ is reached where reduced permeability of the sea ice prevents further rapid desalination. The stable salinity has been considered to vary with ice growth rate; more brine becomes trapped in the ice matrix at higher sea ice growth rates, leading to higher stable salinities [Wakatsuchi and Ono, 1983]. Interior desalination continues at a slower rate following interface desalination as long as the ice remains permeable; the rate of desalination depends on the resistance to fluid flow created by the geometry of connected brine pockets and tubes [Cox and Weeks, 1975; Golden *et al.*, 2007]. We note that these two classes of desalination have been shown to be indistinct in terms of mechanism (i.e. gravity drainage [Notz and Worster, 2009]), however they are useful here to describe the large differences in desalination rate typically found between sea ice freezing at the seawater interface versus the sea ice interior.

[27] Our model uses the same two desalination classes but instead of restricting their use to the ice-seawater interface and interior portions of the ice pack, our hybrid model can apply either desalination method to any layer of sea ice. A simple two-part test determines which desalination method to use. In a given ice layer, if the brine fraction is either less than a threshold value (ϕ_{crit}) or the layer has

reached a stable salinity, we consider the ice not to be slushy and apply the Cox and Weeks [1988, hereinafter CW88] empirical gravity drainage formula for calculating the bulk salinity change in interior ice,

$$\frac{dS}{dt} = \Delta T(A + B\phi_b) \quad (12)$$

where ΔT is the temperature gradient between adjacent layers (K cm^{-1}), ϕ_b is the brine fraction of the ice layer, $A = 1.68 \times 10^{-5}$ ($\text{psu K}^{-1} \text{s}^{-1}$), and $B = -3.37 \times 10^{-7}$ ($\text{psu K}^{-1} \text{s}^{-1}$). Through the dependence on brine fraction (ϕ_b), this parameterization represents a permeability-mediated process since sea ice permeability increases with porosity.

[28] If the brine fraction exceeds ϕ_{crit} in a particular layer, and the bulk salinity is higher than the calculated stable salinity, then we consider the ice to be slushy, and assume that the rate of desalination is instead controlled by the ice growth rate. In this case, we use the stable salinity relationship summarized by Petrich *et al.* [2006] for ice interface growth to determine the bulk desalination rate, derived from Cox and Weeks [1975, 1988]. The stable bulk ice salinity (S_s) is calculated as

$$S_s = k_{eff}S_b, \quad (13)$$

where the stable salinity parameter k_{eff} [dimensionless] is determined experimentally as a power law relationship of dh/dt (m s^{-1}) and a velocity coefficient 1.35×10^{-7} (m s^{-1})

$$k_{eff} = 0.19 \left(\frac{dh}{dt} \frac{1}{1.35 \times 10^{-7}} \right)^{0.46}. \quad (14)$$

[29] Assuming a constant brine salinity, the change in bulk salinity for a freezing region of sea ice by displacement of brine out of an ice layer of thickness z is

$$\frac{dS}{dt} = (1 - k_{eff}) \frac{S_b}{z} \frac{dh}{dt}. \quad (15)$$

[30] Using the stable salinity scheme, calculation of dh/dt is not straightforward since the heat required to freeze sea ice depends on k_{eff} , which is in turn circularly dependent on dh/dt . Modelers have traditionally sidestepped this issue by assuming a fixed q_f at the bottom of the ice, and generally achieve accurate ice growth rates [Bitz and Lipscomb, 1999]. As a workaround to estimate dh/dt for interior ice, we note that the stable salinity relationship can be exploited to estimate the latent heat of freezing (q_f) for an accreted volume of sea ice. Because the stable salinity relationship predicts the salinity at a particular ice growth rate, we can calculate the volume of ice frozen during a time step and derive a minimum heat flux. Assuming the layer conductive heat flux equals q_f (i.e. all extracted heat freezes ice rather than lowers temperature), we construct a relationship between the conductive heat flux F_c and dh/dt (Figure 3). We use two different least square regressions to approximate the relationship between dh/dt (cm s^{-1}) and F_c (W m^{-2}); one polynomial is more accurate at heat fluxes below 57.31 W m^{-2} , which is the case for desalination of most slush layers. There are no data concerning

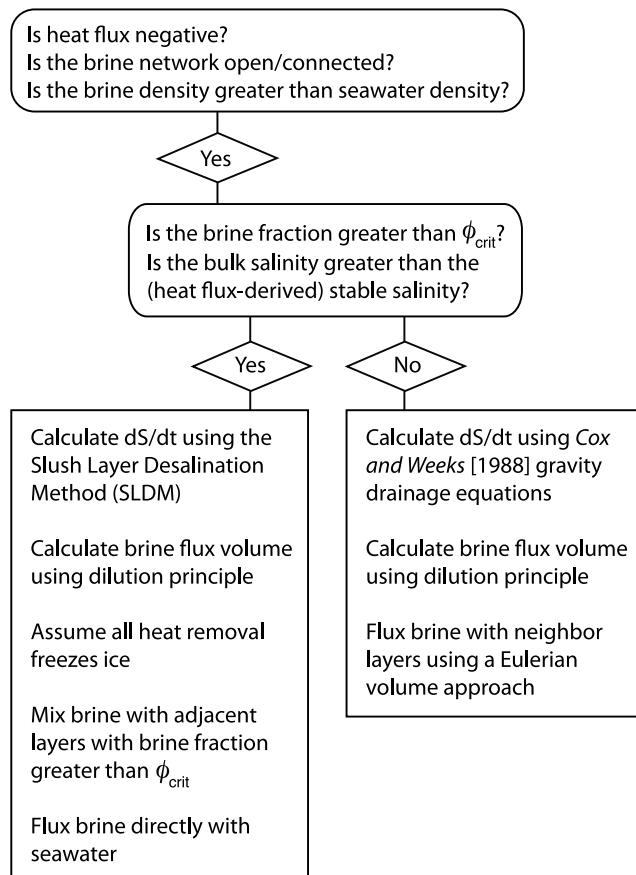


Figure 4. Operational diagram of the desalination scheme.

k_{eff} below $2 \times 10^{-6} \text{ m s}^{-1}$, and growth rates above $2 \times 10^{-4} \text{ m s}^{-1}$ are rarely encountered; therefore, we cap predicted growth rates at these values.

$$\begin{aligned}
 dh/dt &= 5 \times 10^{-6} & F_c < 15.3 \\
 dh/dt &= 1.45 \times 10^{-9} F_c^2 + 3.54 \times 10^{-7} F_c^2 + 5.21 \times 10^{-8} F_c & 15.3 \leq F_c < 57.3 \\
 dh/dt &= 1.94 \times 10^{-13} F_c^4 - 6.00 \times 10^{-11} F_c^3 + 7.39 \times 10^{-9} F_c^2 + 1.76 \times 10^{-7} F_c & 57.3 \leq F_c < 210.0 \\
 dh/dt &= 2 \times 10^{-4} & F_c \geq 210.0
 \end{aligned} \tag{16}$$

[31] Numerical coefficients from polynomial regression have units of $[\text{s m}^{2n} \text{ cm}^{-1} \text{ W}^{-n}]$, where n equals the exponent on F_c to which the coefficient is multiplied. F_c is calculated from the temperature gradient and thermal conductivity across an individual grid layer as $F_c = \Delta T k_i$, using the same space-centered staggered-grid method used in the heat conduction discretization. Positive F_c is in the upward direction. Henceforth, we refer to this slush layer desalination method as SLDM. An operational diagram of the desalination and fluid transport scheme is shown in Figure 4.

[32] We note that the empirical parameterization for k_{eff} was derived from ice accreted to the bottom of the ice sheet, and may not be applicable at temperatures lower than seawater freezing temperatures. However, ice temperatures

close to that of the underlying seawater are required to achieve large brine volumes. Therefore, equations (13)–(16) are only invoked at brine temperatures close to that of seawater. As such, equation (16) provides a reasonable estimate of the accreted ice volume in the sea ice interior from which to estimate desalination.

[33] Typical models of sea ice heat conduction, including the model of *Bitz and Lipscomb* [1999] used here, do not account for changes in sea ice heat content due to desalination and associated changes in latent heat from changes in ice fraction. Without accounting for the latent heat flux associated with replacing brine with ice during desalination, such models can allow freezing fronts to propagate too quickly through desalinating ice. To simulate observed steep temperature gradients and slow freezing front propagation in ice desalinating via SLDM, we assume that latent heat flux accounts for all changes in the heat content of desalinating layers with a brine fraction above ϕ_{crit} , and hold the temperature constant. The treatment of these slush layers is analogous to the treatment of the bottom of the ice column, where the interface temperature is fixed at the seawater temperature [*Maykut and Untersteiner*, 1971; *Bitz and Lipscomb*, 1999].

2.7. Brine Transport

[34] The total salt content of a particular layer of sea ice is only acted upon by the desalination routine. Therefore, after desalination is calculated independently for each layer, we simply remove an equivalent amount of salt from the bulk salinity (CW88). Immediate salt removal is a simplification given the observed motion of brine into and out of sea ice [*Niedrauer and Martin*, 1979; *Wakatsuchi and Ono*, 1983], however the length of model time steps, as well as a lack of high frequency observations of salt motion within sea ice, preclude a more detailed treatment of salt movement. Other tracers, such as nutrients and detritus, are further modified by biology and we account for them differently using a fluid

transport scheme described below. Algae are considered motile and do not move as a result of brine convection (see section 2.5).

[35] In the present model, the desalination and fluid flux equations are not coupled to the heat transfer equation. The brine and ice in any given layer are assumed to be in thermal equilibrium, and the convective heat flux associated with the replacement of colder brine by warmer seawater is ignored. In the cases modeled here, the latent heat flux associated with freezing ice dwarfs any potential convective flux since the temperature difference between the brine and underlying seawater was small ($<0.15^\circ\text{C}$, derived from seawater and brine salinities in the work of *Lytle and Ackley* [1996]). In cases where slush layers are much colder than the underlying seawater [*Sturm et al.*, 1998], convection could be an important determinant of the physical ice state. We explore

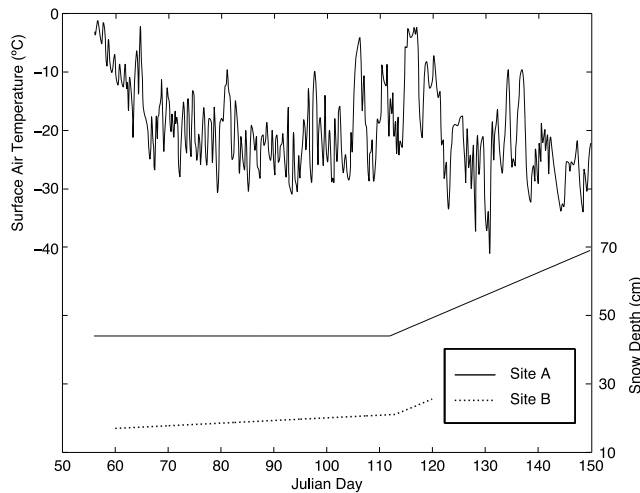


Figure 5. Measured surface air temperature and observed snow depths at Ice Station Weddell used as forcing data for model simulations. Surface air temperature was used at both Site A and Site B. Snow depths were calculated using accumulation rates estimated between day 56 to 112, and 112 to 150 [Ackley *et al.*, 1996].

the biophysical implications and modeling strategies of cold slush layers in the discussion.

[36] The fluid flux during desalination is calculated from the desalination rate using a simple dilution scheme involving the layer below. Underlying this method is the assumption that during a given model time step, brine exiting the layer is removed from the ice to the ocean and is replaced by an equivalent volume of brine from the layer below. Assuming the brine volume is constant in layer i over a time step, the change in salinity is equal to the product of the change in brine salinity with respect to the layer below, and the brine fluid flux F_b (m s^{-1}):

$$\frac{dS^i}{dt} = F_b^i \frac{(S_b^{i+1} - S_b^i)}{z}, \quad (17)$$

where $i + 1$ denotes the layer below. Since the model time step is relatively short, and recognizing that the volume of new ice frozen is not necessarily linked to the amount of brine convected, we ignore the volume expansion associated with freezing new ice. Solving for F_b gives

$$F_b = \frac{dS}{dt} \frac{z}{\Delta S_b} \quad (18)$$

with ΔS_b equal to the difference in brine salinity between convecting layers. For the bottom layer of ice, and when layer brine fraction is greater than ϕ_{crit} , seawater salinity is used in place of S_b^{i+1} in the calculation of F_b . Because equation (18) is unstable at the small differences in brine salinity typically found between model ice layers, we impose a minimum threshold on ΔS_b . This effectively makes ΔS_b a tunable parameter for governing fluid flux, whose impact is explored through sensitivity analysis.

[37] Fluid transport is handled differently under the two desalination parameterizations. In model layers with a brine fraction less than ϕ_{crit} , F_b is calculated using equation (18)

based on desalination derived from CW88. Because the dense brine is observed to exit from brine tubes, we assume that brine exiting a particular layer induces an equivalent exchange in all the layers below, and consequently, the total convective volume in a layer is the sum of that induced by desalination in that layer as well as the layers above. F_b is then used to model the mass transport of solutes using Fick's law [Arrigo *et al.*, 1993], solved using a volume-based first-order accurate discretization.

[38] Ice with a brine fraction above ϕ_{crit} desalinates much more quickly using the SLDM, resulting in larger calculated brine volume fluxes (F_b) using equation (18). High brine fluxes are associated with large-diameter brine tubes up to 0.02 m across that occupy up to 15% of the horizontal ice cross-section [Fritsen *et al.*, 1994]. Beneath a rapidly desalinating layer, such as flooded snow-ice, we assume that brine moves quickly through large brine tubes and bypasses the bulk of the brine matrix in underlying layers, arriving constitutionally intact to the site of desalination. Under the same assumption, dense brine exiting the desalination region quickly leaves the ice through brine tubes with little effect on the layers below. Accordingly, we use a simple volume replacement scheme to mix nutrients into this region of rapid desalination, where an amount of seawater equal to F_b replaces an equal amount of the layer brine, leading to the solute mass balance

$$\frac{dC}{dt} = \frac{F_b}{z} (C_{sw} - C) \quad (19)$$

where C is the brine solute concentration and C_{sw} is the seawater solute concentration. If multiple continuous layers exist with a brine fraction greater than ϕ_{crit} , we assume that they share a fully-mixed brine.

3. Ice Station Weddell Site B Simulation

3.1. Observations

[39] The Ice Station Weddell (ISW) experiment examined the physical and biological processes during fall at a drifting pack ice station in the Weddell Sea. At the ISW Site B study location (hereinafter ISWB), a 0.22 m layer of flooded slush, ~50% liquid by volume, froze under autumn conditions near the surface of a 1.2 m thick snow-covered first year ice pack. Freezing was initiated by rapidly dropping air temperature at the beginning of the study period (Figure 5). The freezing event, as measured by a thermistor string, lasted ~14 days, during which time the freezing front moved progressively downward through the slush layer. From an initial bulk salinity of 18 psu, the slush layer salinity was reduced to 6 psu by the end of the 14 days. The air temperature, ice temperature profile, ice and snow thickness, dissolved inorganic nitrogen (DIN) concentration, and ice algal pigment concentration were monitored over the course of 60 days [Fritsen *et al.*, 1994; Lytle and Ackley, 1996; Ackley *et al.*, 1996].

3.2. Initial Conditions

[40] Our simulation covers days 60–120 during the ISWB period, and is initialized with a 0.22 m slush layer beginning 0.08 m below the ice surface (Figure 6). The salinity of the 0.08 m layer of ice above the slush layer varies linearly

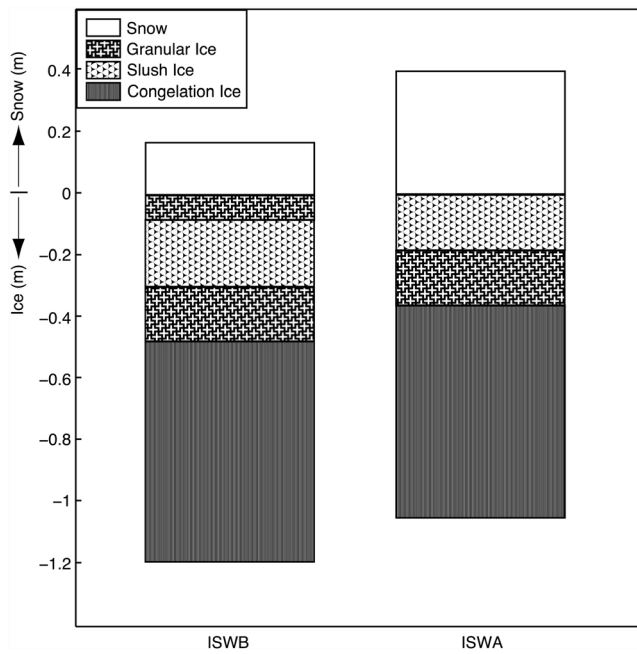


Figure 6. Vertical diagram of the different ice types used as initial conditions for ISWB and ISWA simulations (scale in m).

between 6 psu at the surface and 18 psu at the slush layer, a gradient we inferred from the observation that freezing had started before observations began on day 60. The slush layer itself is assigned the salinity of 18 psu [Lytle and Ackley, 1996]. Below the slush layer was a granular ice layer 0.18 m thick, to which we assigned a salinity of 8 psu. Congelation ice was below the granular layer, where we initialized salinities according to a standard C-shape salinity profile (ca. 4–5 psu, Table 4 [Arrigo and Sullivan, 1994]) that correspond to measured salinities of first-year ice [Melnikov, 1998]. The initial ice temperatures were derived from the ISWB thermistor data.

[41] Initial snow depth at ISWB was set at 0.17 m on day 60, with snowfall accumulation thereafter consistent with rates measured at ISWB (0.8 mm day^{-1} between day 60 and 112 and 6.5 mm day^{-1} during day 112–120 [Lytle and Ackley, 1996, Figure 5]). The thermal conductivity of snow (k_s) was set at $0.4 \text{ W g}^{-1} \text{ K}^{-1}$ to achieve the observed rates

Table 4. Thickness-Dependent Salinity Values (psu) Used to Derive Initial Salinity Profiles for Model Runs, With Initial Ice Thickness h

Ice Thickness	Bulk Ice Salinity
0	8
$h/9$	6.3
$2h/9$	5.6
$3h/9$	5.3
$4h/9$	5.2
$5h/9$	5.1
$6h/9$	4.9
$7h/9$	4.8
$8h/9$	4.8
H	6.2

Table 5. Forcing Data Sources

Forcing Data	Source
Air Temperature	Measured ^a
Wind Speed	ECMWF ^b
Humidity	ECMWF ^b
Surface Air Pressure	ECMWF ^b
Cloud Cover	ECMWF ^b
Ocean Heat Flux	Measured ^a
Snow Depth	Measured ^a
Initial Ice Salinity	Measured ^{a,c}
Water Column Properties	Measured ^{a,c}

^aLytle and Ackley [1996].

^bECMWF Interim Reanalysis.

^cMelnikov [1998].

of cooling, especially after slush layer desalination. This value of k_s is higher than is typically used when modeling snow, but is justified by the multiple re-frozen, dense, icy layers observed in the ISW snow pack that conduct heat more quickly than loose snow [Lytle and Ackley, 1996; Sturm et al., 2002]. Further physical forcing data are listed in Table 5.

[42] Algal concentration was initialized to 200 mg C m^{-3} across the slush layer and underlying granular layer, and to 35 mg C m^{-3} elsewhere in the ice. The initial column integrated algal biomass was $2.88 \text{ mg Chl } a \text{ m}^{-2}$, which was concentrated in the high brine fraction layers, consistent with observed values of $2.3\text{--}5.2 \text{ mg Chl } a \text{ m}^{-2}$ [Fritsen et al., 1994]. Because water column nutrients were close to deep water values, we fixed the model water column nutrient concentrations at $30 \text{ } \mu\text{M NO}_3$, $2 \text{ } \mu\text{M PO}_4$, and $80 \text{ } \mu\text{M Si(OH)}_4$. Initial water and ice column NH_4 and POC concentrations are assumed to be zero. The nutrient concentrations in brine were initialized to 20% of seawater values, as observed by Fritsen et al. [1994].

3.3. Model Runs

3.3.1. Standard Run (Run W1)

[43] The new parameters introduced into the model by our desalination and fluid transfer scheme are the critical brine fraction (ϕ_{crit}) that determines which of the two desalination and fluid transfer methods will be used, and the minimum difference in brine salinity (ΔS_b) that is used to calculate the brine flux volume (Table 6). During model development, we first tuned ϕ_{crit} until modeled slush layer salinity, temperature, and algal biomass most closely matched observations. The parameter ΔS_b is relatively independent, and was tuned after ϕ_{crit} to match estimates of brine flux made by Fritsen et al. [1994] and Ackley et al. [1996]. Based on this model tuning and sensitivity analysis (presented below), values of 0.2 for ϕ_{crit} and 2 psu for ΔS_b result in the best overall fit to observed data.

3.3.2. Sensitivity to ϕ_{crit}

[44] We examine model response to variation in ϕ_{crit} , including setting it higher (0.25; run W3) and lower (0.15; run W2) than the standard run value, turning off SLDM and replacing it with CW88 (run W4). We also allow desalination of ice layers as in the standard run while neglecting the associated latent heat flux (W5).

3.3.3. Sensitivity to ΔS_b (Runs W6–W9)

[45] This parameter directly controls the brine flux volume, which determines the amount of nutrients available to

Table 6. ISW Model Runs and Parameters

Run	Simulation	Desalination Latent Heat	ϕ_{crit} (Fraction)	ΔS_b (psu)	Initial Slush Layer (m)	Grid Thickness (m)
W1 ^a	ISWB	yes	0.2	2	0.22	0.01
W2	ISWB	yes	0.15	2	0.22	0.01
W3	ISWB	yes	0.25	2	0.22	0.01
W4	ISWB	yes ^b	–	2	0.22	0.01
W5	ISWB	no	0.2	2	0.22	0.01
W6	ISWB	yes	0.2	1	0.22	0.01
W7	ISWB	yes	0.2	1.5	0.22	0.01
W8	ISWB	yes	0.2	2.5	0.22	0.01
W9	ISWB	yes	0.2	3	0.22	0.01
W10	ISWB	yes	0.2	2	0.22	0.02
W11	ISWB	yes	0.2	2	0.22	0.05
W12	ISWB	yes	0.2	2	0.22	0.10
W13 ^a	ISWA	yes	0.2	2	0.18	0.01
W14	ISWA	yes	0.15	2	0.18	0.01
W15	ISWA	yes	0.25	2	0.18	0.01
W16	ISWA	yes ^b	–	2	0.18	0.01

^aStandard run.

^bLatent heat flux derived CW88 desalination only (all other runs derived from CW88 and SLDM when employed).

sea ice algae growing in a slush layer. These model runs encompass variations in ΔS_b between 1 and 3 psu.

3.3.4. Sensitivity to Vertical Resolution (Runs W10-W12)

[46] To test the ability of our model to simulate slush layer dynamics at the lower vertical resolution typical of global-scale models, we ran the model at layer spacings of 0.02, 0.05, and 0.1 m, in addition to the standard run at 0.01 m. We note that many models actually use even larger effective grid sizes, representing sea ice with just 1–4 layers [Flato and Hibler, 1995; Zhang and Rothrock, 2003; Lipscomb and Hunke, 2004]. However, if surface flooding and other slush layer-generating mechanisms are to be included in such models, resolution of at least the slush layer itself will need to be increased. With fewer layers, the average brine fraction of a layer containing a slush layer would be too low, and consequently, would not trigger the appropriate rapid desalination and convection routines.

3.4. Results

3.4.1. Standard Run

[47] The ISWB standard run (run W1) simulation matches measured temperature profiles extremely well, with an error that is generally far less than 1°C (Figures 7 and 8a). The model tracks the observed -2°C isotherm accurately as the freezing front advances slowly through the slush layer (days 60–74) and as it accelerates after propagating past the slush layer on day 74, due to more rapid cooling.

[48] The modeled uppermost ice cools slightly faster than observations during the freezing of the slush layer. This can be attributed to the SLDM and associated latent heat flux, which tends to desalinate the slushy regions progressively downward, one layer at a time. In reality, the entire slush region may desalinate at once, as convecting brine may distribute the heat flux across entire slush region, resulting in slightly higher observed temperatures near the ice surface when compared to model results. After day 74, modeled and observed isotherms are in better agreement at the ice surface.

[49] The slush layer desalinates rapidly according to the SLDM during the first 14 days of simulation. Desalination

slows as brine volumes drop below ϕ_{crit} after day 74, after which model desalination is governed by CW88. The mean salinity of the slush layer on day 74 is 6.6 psu and is further reduced to 6.3 psu before desalination is cut off completely due to declining temperature and brine fraction (Figure 8b). This final slush layer bulk salinity agrees well with the observed value of 6 psu.

[50] Total daily fluid transport shows a sharp decline after the slush-layer freeze-up on JD 74 (Figure 8c). The total fluid replacement in the slush layer during the first 15 days of the simulation for the standard run was $1.14 \text{ m}^3 \text{ m}^{-2}$ or $0.076 \text{ m}^3 \text{ m}^{-2} \text{ day}^{-1}$, equating to a 10.4x turnover rate over the course of the slush layer desalination. This fluid flux is in the middle of the range of brine volume flux ($0.8\text{--}1.8 \text{ m}^3 \text{ m}^{-2}$) estimated using a salt-balance approach during slush layer freezing at ISWB [Ackley *et al.*, 1996].

[51] Although the model includes a number of different nutrients, we restrict our discussion to nitrate since it is the first nutrient to limit algal growth in our model. Nitrate values in bulk sea ice, initially at 20% of seawater concentration, increase rapidly once desalination of the slush layer begins, and brine nutrient concentrations become equivalent to seawater values by day 63, just three days after the simulation begins (Figure 9a). Algae, although increasing exponentially, are not able to reduce nutrient concentrations until after the slush layer freezes. Above the freezing front, desalination and fluid flux slow nutrient replenishment and resident algae quickly consume the remaining nitrate, leading to a downward progression of nitrate exhaustion in the slush layer.

[52] Algal biomass accumulates most rapidly during the first three weeks of the simulation, in agreement with observations (Figure 8d). After the freezing front passes, the convection-driven nutrient supply is cut off, and algae

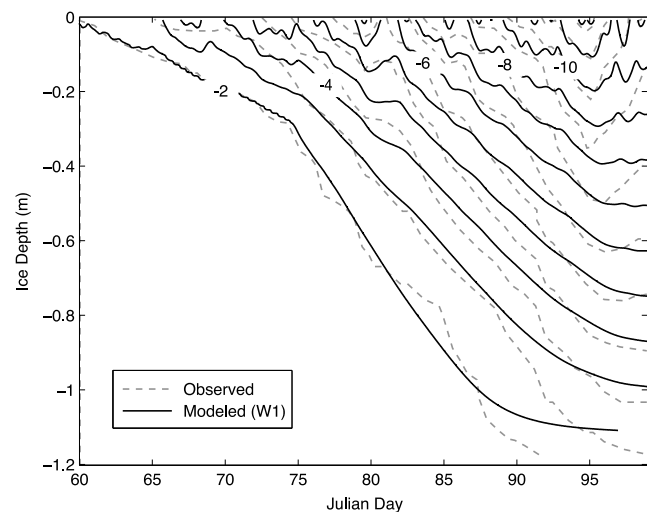
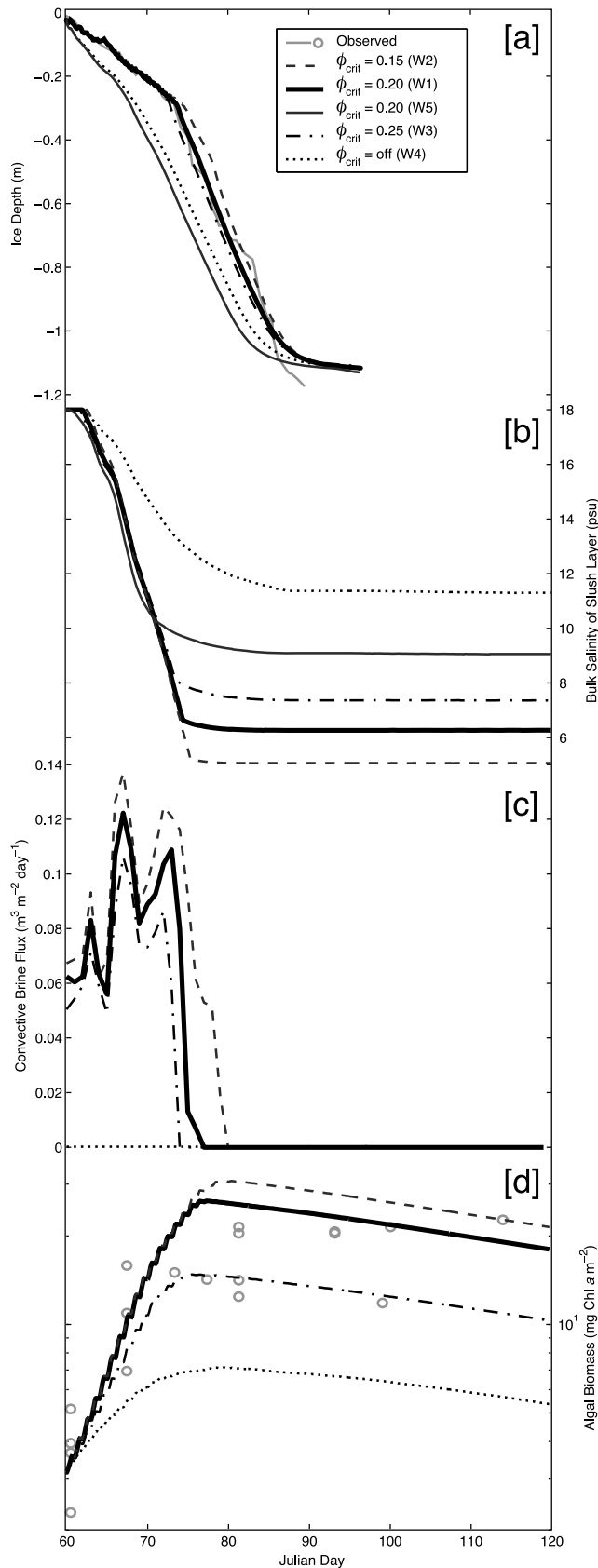


Figure 7. A comparison of observed and modeled temperature contours within the ice pack over time at ISW Site B ($^\circ\text{C}$). The model reproduces the initial freezing front as it passes through the slush layer located between -0.07 to -0.29 m depth. Beyond day 74 the ice cools more rapidly from the top as brine convection becomes less significant. The model underestimates cooling later in the simulation by up to 1°C .



quickly become nutrient limited. The maximum column-integrated biomass of 25 mg m^{-2} reached during the bloom is within the range of $20\text{--}27 \text{ mg Chl } a \text{ m}^{-2}$ measured at ISWB. Algal concentrations were highest ($84 \text{ g Chl } a \text{ m}^{-3}$) in the frazil ice below the slush layer (Figure 9b); continued flushing of this region by seawater nutrients, in conjunction with a later freeze date, allowed optimal growing conditions below the slush layer to persist longer than anywhere else in the ice. Cold temperatures and low nutrients restrict algal growth after day 78 and there is no further algal biomass accumulation.

3.4.2. Sensitivity to Slush Layer Desalination and ϕ_{crit}

[53] The simulation that employed CW88 instead of SLDM in the slush layer (run W4) failed to replicate any of the temperature, bulk salinity, nutrient, or biomass observations. The freezing front passes too rapidly through the slush layer by day 69, ~ 5 days earlier than observed (Figure 8a). More importantly, the exclusive use of CW88 only reduces salinity to ~ 12 psu in the first 14 days (Figure 8b), and because brine flux is small, nutrient levels do not increase enough to stimulate a large enough ice algal bloom. Maximum algal biomass accumulation is just $6.8 \text{ mg Chl } a \text{ m}^{-2}$, less than one third of observed values (Figures 8d and 9b).

[54] When ϕ_{crit} is lowered from 0.2 to 0.15 (run W2), the slush layer cools too slowly and delays the transit of the -2°C isotherm through the slush layer (Figure 8a). In addition, more salt is rejected from the slush layer so that it arrives at a final bulk salinity of 5 psu, 1 psu lower than the observed value (Figure 8b). Chl *a* concentrations follow a similar growth trajectory but the algae reach a higher than observed Chl *a* concentration of $30.3 \text{ mg Chl } a \text{ m}^{-2}$, since nutrients are replenished via intense brine convection over a

Figure 8. Time series of ISWB observations and modeled physical and biological parameters with varied ϕ_{crit} . (a) Depth of the ISWB freezing front over time for different values of ϕ_{crit} as demonstrated by the -2°C isotherm. By either ignoring the latent heat associated with desalination or without the SLDM ($\phi_{crit} = \text{off}$) the freezing front proceeds too quickly downward through the ice. The standard run ($\phi_{crit} = 0.20$) fits the observed data reasonably well; with $\phi_{crit} = 0.25$ appears to be a slightly better fit, however using $\phi_{crit} = 0.20$ results in salinities and algal growth that more closely matches observations. (b) Evolution of modeled slush layer salinity over a range of critical brine fractions (ϕ_{crit}). Once freezing of the slush layer begins, rapid desalination causes the bulk salinity to decrease rapidly until completion of freezing on day 74. In the case of $\phi_{crit} = 0.20$, the salinity decreases to close to 6 psu, in line with observations. In the case of only CW88 interior ice desalination ($\phi_{crit} = \text{off}$), the salinity decreases much more slowly, and never reaches below 13 psu. (d) Daily convective brine flux volume during ISWB simulations with varied ϕ_{crit} . Fluxed volumes respond negatively when the slush desalination scheme is used over a smaller range of brine volumes (increases in ϕ_{crit}). (c) Total ISWB ice column Chl *a* concentration observed and modeled using a range of ϕ_{crit} . Simulations stopped at day 120. Without using the slush desalination scheme, algal growth is stunted by a lack of nutrients and algal biomass does not reach any of the observed values (run W4). Using $\phi_{crit} = 0.20$ best reproduces the observed Chl *a* concentration over time.

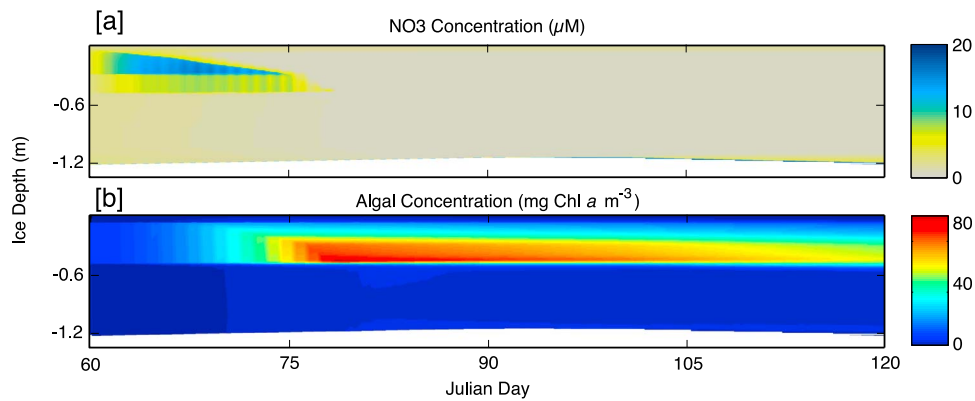


Figure 9. ISWB sea ice model depth profile evolution over time of (a) NO_3 concentration and (b) algal biomass. Overlying snow is not shown. As the slush layer is cooled from above, it desalinates and freezes. The desalination induces rapid brine exchange during the freezing period and mixes in nutrients into the porous ice. The nutrient supply is largely cut off by day 75 after the slush layer freezes, and algae reach their peak biomass after exhausting the nutrients ~ 7 days later.

longer period of slush layer desalination (Figure 8d). The brine flux volume maintains a pattern similar to the standard run, but is consistently higher, reflecting the additional desalination (Figure 8c).

[55] With ϕ_{crit} elevated from 0.20 to 0.25 (run W3), the slush layer desalination scheme is stopped at a higher brine fraction than in the standard run, and the freezing front descends more rapidly through the slush layer (Figure 8a). Although, the -2°C isotherm more closely tracks the observed data than in the standard run, the standard run exhibits salinities and algal growth rates that more closely match observations (Figures 8a and 8d). The bulk salinity of the slush layer remains above 7.8 (Figure 8b), higher than the observed value of 6 psu, and the brine flux volume is reduced, reflecting the reduced desalination (Figure 8c). Chl *a* accumulation is reduced from the standard run due to colder temperatures from earlier freezing front advancement, and more importantly, due to shorter duration of significant brine convection, which reduces influx of nutrients. The maximum integrated algal biomass of $14.2 \text{ mg Chl } a \text{ m}^{-2}$ is 37% below observations (Figure 8d).

[56] To examine interplay between the salt and heat components of the SLDM, in run W5 we ignored the change in latent heat associated with replacement of brine with new ice during desalination. When $\phi_{crit} = 0.2$, as in the standard run, the freezing front proceeds too fast through the slush layer (Figure 8a), indicating that consideration of both salt and heat fluxes are required to reproduce observations. Here, the slush layer freezes even faster than the case without SLDM (W4), since ice with a lower salt content has a smaller effective specific heat (q_b).

3.4.3. Sensitivity to ΔS_b

[57] Because the brine flux volume is independent of the convective heat flux estimate, varying ΔS_b does not impact ice physics beyond the transport of brine and associated nutrients. However, different nutrient concentrations caused by differences in the amount of total fluid flux have the potential to impact algal growth. The total brine flux volume increases with a decreasing ΔS_b (Table 7). Reducing ΔS_b by 50% to 1 psu (run W6) effectively doubles the brine transport, and conversely, increasing ΔS_b (runs W8-W9) results

in a lowering of brine transport. Convection is vigorous in all runs, however, and nutrient supply to the algae is not limiting in any of these test cases with respect to the standard run. Biomass accumulation is largely unaffected and, therefore, these results are not shown. In the case of ISWB, it seems that biological growth cannot be used to further constrain the physical fluid flux.

3.4.4. Sensitivity to Vertical Resolution

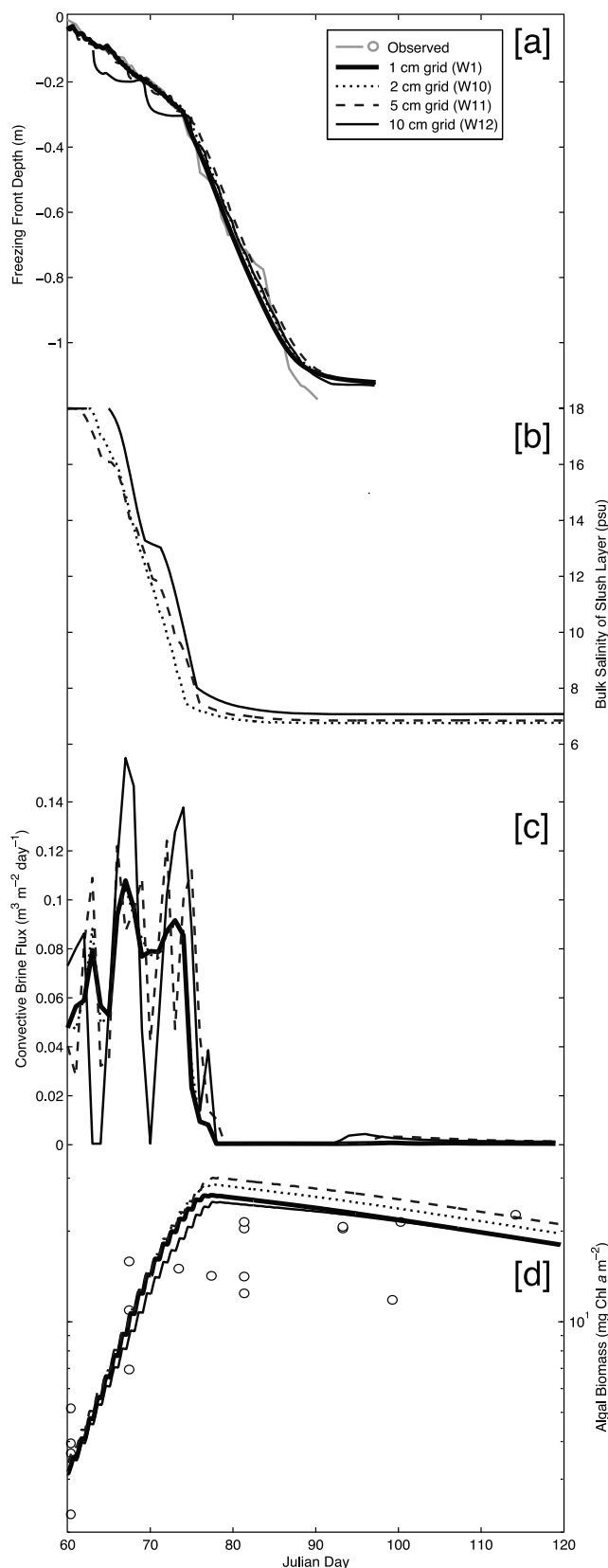
[58] Overall, model results are remarkably consistent for different vertical resolutions (Figure 10). The transition from slower freezing of the slush layer to faster freezing of the solid ice below at day 74 is captured at all resolutions (Figure 10a), although at increased layer thickness, a step-like form is visible in the progression of slush layer freeze up. These steps result when the layer brine fraction crosses the ϕ_{crit} boundary and the desalination method is switched from SLDM to CW88. Despite the stepping, even when the slush layer is composed of just two layers, as in the case of the 0.10 m simulation (run W12), the average freezing rate is still simulated with reasonable accuracy.

[59] Furthermore, most model runs arrive at a similar bulk salinity after desalination (Figure 10b), with the final slush layer salinity being only slightly higher when 0.1 m thick layers were used (6.7 psu) than in the standard run with 0.01 m thick layers (6.3 psu; run W1). At increased layer thickness, extra cooling is required before desalination begins and because the layer is slightly colder when the brine fraction reaches ϕ_{crit} , the brine salinity is higher.

Table 7. Integrated Convective Brine Flux Volumes for ISWB Simulations Using Different Values of the Minimum Inter-layer Brine Salinity Difference

ΔS_b (psu)	Brine Flux Volume (m^3)
1	2.37
1.5	1.58
2	1.18
2.5	0.95
3	0.79

[60] The variability in brine flux increases markedly with decreasing vertical resolution, and in the 0.1 m case, ceases altogether for a day around day 63 as the freezing front passes between model layers (Figure 10c). Due to the similar



bulk salt content and freezing rate, however, the total integrated brine flux is similar for all runs, varying between 1.14 and $1.31 \text{ m}^3 \text{ m}^{-2}$.

[61] Regardless of vertical resolution, the modeled fluid flux is sufficient to supply algae with ample nutrients to fuel growth during slush layer desalination. Because of the continued flushing, algae are able to grow at their physiological maximum, encountering nutrient limitation only after the slush layer has frozen. This leads to similar algal biomass accumulation between simulations with a different vertical resolution (Figure 10d). In fact, decreasing vertical resolution results in slight overestimates of maximum seasonal biomass, with biomass in the 0.1 m resolution run exceeding by 20% the value of $25.2 \text{ mg Chl } a \text{ m}^{-2}$ reached in the standard 0.01 m run. Total Chl *a* initially accumulates at the same rate, but algae continue net growth later into the simulation with greater layer thickness. Because slush layers share a mixed brine, algae in the top of a thick grid layer have continued access to nutrients if the freezing front has not passed completely through the layer (i.e. SLDM still active), which leads to elevated growth.

4. ISW Site A Simulation

4.1. Observations

[62] Time series observations at Ice Station Weddell Site A (hereinafter ISWA) include a detailed set of physical and biological ice monitoring data identical in scope to those at ISWB, but in a more varied ice floe where deformation produced a highly heterogeneous ice pack. Observations at ISWA begin on day 56, 4 days earlier than at ISWB, when the ice pack was still isothermal due to very recent surface flooding and warm atmospheric temperatures. Because of the heterogeneous ice pack, different thicknesses of slush were observed depending on the sampling location, with 80% of locations below freeboard. [Fritsen *et al.*, 1994; Lytle and Ackley, 1996; Ackley *et al.*, 1996].

[63] Simulation of observed physical properties from a heterogeneous floe can be difficult using a one-dimensional

Figure 10. Time series of ISWB observations and modeled physical and biological parameters with varied grid size. (a) Depth of the ISWB freezing front over time for different model grid spacing as demonstrated by the -2°C isotherm. Grid size has little effect on the freezing front progression, although ‘stepping’ that occurs when the brine volume is reduced past ϕ_{crit} can be easily seen in the case of the 10 cm grid. (b) Evolution of modeled slush layer salinity over a range of model grid spacing. The modeled salinity is especially sensitive to grid spacing. (c) Daily convective brine flux volume during ISWB simulations with varied model grid spacing. The grid spacing causes the brine flux to be more highly variable on a daily basis, however the total volume fluxed during the simulation (i.e. integration of the above curves) only varies between 1.18 and 1.31 m^3 . (d) Total ISWB ice column Chl *a* concentration observed and modeled using different model grid spacing. Total Chl *a* initially accumulates at the same rate, but algae continue net growth later into the simulation with larger grid spacing. Algae in the top of a thick grid layer have continued access to layer nutrients if the freezing front has not passed completely through the layer, leading to elevated growth.

model. Ice core biomass may vary by several orders of magnitude depending on whether gaps exist in ridged ice, or where large variations in snow depth drastically alter the light available to ice-bound algae. At ISWA, the thermistor string sampled a vertical profile of ice temperatures over time but was likely influenced by nearby ice and snow of varying thicknesses that create horizontal temperature gradients [Sturm *et al.*, 2002].

[64] Nevertheless, observations at ISWA lend confidence that a one-dimensional model can capture the essential evolution of a heterogeneous ice pack. The use of multiple core samples captures some of the variability in observations of algal biomass. Furthermore, the initial thickness of ice (1.1 m) and snow (0.4 m) at the site of the ISWA thermistor

string are within one standard deviation of the mean floe ice and snow thicknesses (1.44 m and 0.44 m, respectively [Lytle and Ackley, 1996]), giving confidence that measured temperatures represent a median for the floe that can be compared to model results.

4.2. Initial Conditions

[65] We assigned an initial slush layer thickness of 0.18 m, the mean slush layer thickness calculated for the ice floe [Lytle and Ackley, 1996]. The depth of the slush layer at the thermistor string is unknown, although thought to be >0.06 m [Ackley *et al.*, 1996]. The temperature records show a delayed freezing front advancement across a depth greater than 0.06 m, indicating that either there was lateral heat transfer from adjacent warm ice (perhaps due to further flooding, or differences in local snow depth) or the actual slush layer was much thicker than 0.18 m (Figure 11a). We assumed the slush layer was above the more solid ice surface having a salinity of 16 psu [Ackley *et al.*, 1996]. Without additional information concerning mean initial ice properties, we prescribed the initial salinity profile similarly to ISWB, with an 8 psu, 0.18 m thick granular layer below the slush layer, and congelation ice below the granular layer with a standard C-shape salinity profile from Table 4 (see Figure 5 for ice column diagram). In accordance with observations, the ice temperature was initially isothermal at the seawater temperature, and a linear temperature gradient in the snow varied from seawater temperature at the bottom of the layer to atmospheric temperature at the top. Nutrients were initialized similarly to the ISWB simulations, and initial algal concentrations were assigned to match observations. The simulation period was from day 56 to 150; air temperature and snow forcing are shown in Figure 6.

4.3. Model Runs

[66] The ISWA standard run (W13) uses the same desalination parameters as the ISWB standard run.

[67] Because the value of ϕ_{crit} that yields results most consistent with observations might differ between ISWA and ISWB, we performed a sensitivity analysis of ϕ_{crit} identical

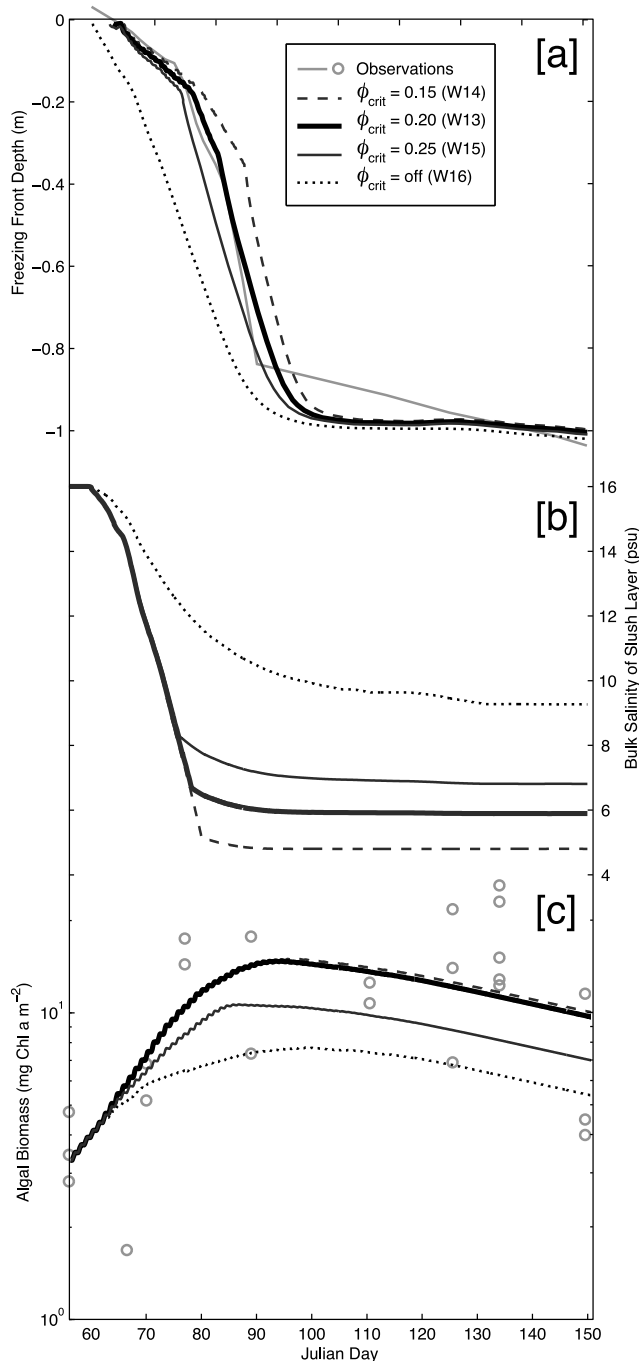


Figure 11. Time series of ISWA observations and modeled physical and biological parameters with varied ϕ_{crit} . (a) Observed and modeled freezing fronts at ISWA. The observed freezing front is the -1.8°C isotherm [Lytle and Ackley, 1996], while the modeled fronts are -1.9°C isotherm. Because the reported seawater salinity is 34.1 psu, model desalination does not begin until the brine salinity reaches above 34.1 psu, which occurs at a temperature of -1.84°C . The isotherm at -1.9°C is a better metric of freezing for the model. (b) Evolution of ISWA modeled slush layer salinity for model run using different values of ϕ_{crit} . Similarly to ISWB results, using $\phi_{crit} = 0.20$ produced the most accurate desalination profile, with salinity reaching 6.2 psu, near the observed value of 6 psu. (c) Total ice column Chl *a* concentration observed and modeled using a range of ϕ_{crit} for ISW Site A. At this site heterogeneous ice conditions produced variable Chl *a* observations. Without the slush layer desalination scheme ($\phi_{crit} = \text{off}$), algal growth to observed values is not achievable. As in the ISWB simulation, a ϕ_{crit} value of 0.20 results in a reasonable approximation of the magnitude of biomass accumulation.

to that for the ISWB simulation. We also performed one model run where the SLDM was turned off and replaced by CW88 (W16), representative of a traditional sea ice model.

4.4. Results

4.4.1. Standard Run

[68] Using the standard value for $\phi_{crit} = 0.20$ in the ISWA run (W13), the simulated depth of the freezing front tracks the observed freezing front reasonably well (Figure 11a). The freezing front does not begin to enter the slush layer until after day 60 due to the insulating snow cover. Temperature observations show a transition from slow to fast cooling around day 75–76, approximately two days earlier than in the model. This transition marks the transit of the freezing front through the slush layer. The two extra days of slush layer freezing in the model is not unexpected since the thickness of the slush layer at the thermistor string may have been thinner than the ISWA floe average of 0.18 m assumed in the model [Ackley *et al.*, 1996]. Using a thinner slush layer in the simulation would likely result in a better match to observed temperatures, but we are interested in how well the model represents observations using mean floe values.

[69] The slush layer desalinated to 6.0 psu after freezing (Figure 11b), matching the observed rate of desalination and final slush layer bulk salinity of 6 psu [Ackley *et al.*, 1996].

[70] Nutrients follow a similar pattern and profile to those at ISWB and are not shown. Nutrients in the slush layer brine, initially below seawater concentrations, increase rapidly and reach near-seawater values as the freezing and desalination of the slush layer begins. Nutrients are quickly exhausted by the large algal biomass once the slush layer freezes.

[71] Algal time series measurements from ISWA show more variability than at ISWB due to the more heterogeneous ice conditions. In the standard ISWA run ($\phi_{crit} = 0.20$), algal biomass increases at a rate consistent with the range of observations (Figure 11c). After reaching a peak biomass at day 85, algal biomass in the model slowly declines for the remainder of the simulation. As in the ISWB simulations, algae exhaust available nutrients shortly after the slush layer freezes and rapid brine convection ceases. After day 120, there is a notable increase in algal biomass at ISWA that is coincident with an extreme warming trend [Ackley *et al.*, 1996]. While the model captures the ice temperature trends, algae in the model are still nutrient starved during the warming period because of a lack of brine convection. Increased sea ice permeability during surface warming may have allowed additional surface flooding or wicking of brine into overlying snow due to coincident snow loading and observed negative freeboards [Lytle and Ackley, 1996]; these processes were not captured by the model but would allow replenishment of nutrients in the ice interior.

4.4.2. Sensitivity to ϕ_{crit}

[72] As in ISWB, a value for ϕ_{crit} of 0.20 resulted in the most realistic simulation of observed data (run W13). Increasing ϕ_{crit} to 0.25 (run W15) resulted in a slightly better match between modeled and observed freezing fronts, although modeled algal biomass was lower than the majority of observations. At $\phi_{crit} = 0.15$ (run W14), the slush layer took several days longer to freeze than in observations and desalinated too quickly and to too low a value (5.1 psu). Moreover, algal biomass was generally higher than the range

of observations. Running the model using only the traditional CW88 desalination scheme (run W16) resulted in unrealistically rapid cooling, overly high salinity, and depressed algal growth when compared to time series observations (Figure 11).

5. Discussion

5.1. Simulating ISW

[73] *Fritsen et al.* [1994] and *Lytle and Ackley* [1996] provide evidence that brine exchange during desalination was a significant source of heat and nutrients to a sea ice slush layer at ISW, which allowed a large algal bloom to develop. We have shown that a traditional model treatment of interior sea ice desalination [CW88; *Maksym and Jeffries*, 2000] under-predicts desalination and brine exchange in slush layers during simulations of ISW sites, which then leads to depressed temperatures, reduced nutrient flux, and ultimately lower rates of algal production compared to observations. Using our new hybrid treatment of ice desalination, we are able to model observed ISW sea ice physics with enough precision to accurately simulate observed algal growth.

[74] The ISW time series data have been previously used for sea ice model development, but these efforts did not include a coupled desalination scheme. *Fritsen et al.* [1998] used the Ice Station Weddell time series data to specify slush layer conditions in a coupled model of sea ice, similar to our study. In their model, the slush layer thermal properties were subject to a separate, non-heat-conservative thermodynamic term that required a porosity estimate, and the ice salinity was invariant at 8 psu. Although this treatment of the slush layer permitted simulation of algal production, the model is not readily portable because the slush layer physics are not predicted. Instead, they are specific to the test case. The same time series observations were also modeled by *Andreas et al.* [2005], where the slush layer was treated similarly to our simulations in that all heat extraction is in the form of freezing sea ice up to a cut-off brine fraction. However, ice salinity, desalination, and brine flux were not explicitly modeled.

[75] Our slush layer desalination and fluid transfer method (SLDM) constitutes a step forward from *Fritsen et al.* [1998] and *Andreas et al.* [2005], where the processes of desalination, brine exchange, and latent heat removal are coupled to sea ice equations of state and conductive heat transfer, allowing most feedbacks between physical, chemical, and biological processes to proceed as observed. The model is able to accurately track large changes in the physical properties of sea ice from highly porous slush to frozen, low brine fraction sea ice with sufficient accuracy to correctly simulate ice algal growth in the sea ice interior. Despite the spatially heterogeneous ice environment at ISWA, the model is able to simulate desalination and ice algal growth close to observed values when using mean initial values of snow and slush layer thicknesses.

5.2. Evidence for Rapid Desalination of Slush Layer

[76] The Ice Station Weddell time series data begin after a large flooding event, followed by a 35-day period of cooling. This intense cooling period allowed continuous desalination of a relatively thick slush layer, a process facilitated

by large, 0.005–0.03 m diameter brine tubes that connected the slush layer and the underlying water column through more consolidated sea ice [Fritsen *et al.*, 1994; Ackley *et al.*, 1996]. Neither the specific conditions under which large brine tubes form, nor their rate of formation, has been observed or determined experimentally. Therefore, it is possible that ice states that are different from those found at ISW, such as a relatively thin slush layer or the absence of an established network of large brine tubes, might discourage rapid slush layer desalination. The presence of a superimposed fresh ice layer in the snow or ice pack might also affect the freeze dynamics of a slush layer by providing a low porosity barrier to convection. In these cases, the permeability of ice, either within or underlying a slush layer, could be significantly different from that at ISW. Errors in slush layer simulation using our model could occur where the SLDM is tuned to ISW observations, notably the rate of desalination (and the value of ϕ_{crit}) and the estimation of the brine flux volume.

[77] Evidence suggests however, that if the seawater can find a path to flood the sea ice surface, then it can also find a way to exit again as more saline brine is formed. Hudier *et al.* [1995] describe observations of sea ice following a storm where the surface flooded and the resulting slush layer cooled over the course of several hours. After an initial rapid cooling to -2.32°C , the temperature of the slush layer warmed over the course of five hours to -1.7°C , despite air temperatures of -5 to -10°C , indicative of convection between the ocean and the slush layer. As such, fluid pathways adequate for rapid convective exchange with underlying seawater must have been established in the first few hours after flooding. The observed salinities of frozen slush layers, or snow ice, support our estimate of initially vigorous slush layer desalination as well. Measured bulk ice salinities of snow ice can average 6.5 psu in the Arctic and 9.3 psu in the Antarctic [Maksym and Jeffries, 2001]. If slush layer desalination normally takes place more slowly than observed at Ice Station Weddell, one might expect to see average bulk salinities closer to that of the initial slush layers (~ 17 – 24 psu [Hudier *et al.*, 1995; Lytle and Ackley, 1996; Fritsen *et al.*, 2001]).

[78] Micro-scale simulations of snow ice formation and physical evolution by Maksym and Jeffries [2001] generally validate our efforts. During freezing of flooded snow, their model showed how thermohaline convection of brine can dissolve new brine channels through less permeable underlying ice. Creation of such channels, while allowing rapid brine convection and desalination, caused minimal changes to the bulk salinity of the underlying ice, consistent with our model assumptions. Furthermore, their simulations suggest an initial desalination rate of slushy sea ice that is higher than predicted by CW88.

5.3. Model Applicability

[79] Under conditions of slow freezing common to interior slush layers, using $\phi_{crit} = 0.2$ to determine switching from the fast desalination of the SLDM to the slower desalination of CW88 essentially limits overall desalination to values near 6 psu. As described in the methods, it is necessary to limit the use of the SLDM to conditions of elevated porosity via the ϕ_{crit} parameter to achieve the measured ISW bulk salinities in the slush layer after freezing. Without the use of

ϕ_{crit} the SLDM will desalinate ISW slush ice to the ‘stable salinity’ estimated for congelation ice (~ 4 psu [CW88; Petrich *et al.*, 2006]), which is lower than observed values of bulk salinity for the frozen slush layer at ISW (6 psu [Fritsen *et al.*, 1994; Ackley *et al.*, 1996]).

[80] The general use of ϕ_{crit} calculated from ISWB data using our model is defensible based on a recent study of sea ice permeability. Golden *et al.* [1998] and K. M. Golden (manuscript in preparation, 2012) suggest that granular ice permeability may be smaller than congelation ice permeability at a given porosity. Because slush layers demonstrate granular ice structure after freezing [Sturm and Massom, 2009], we propose that interior layers of slushy sea ice might desalinate more slowly at moderate brine volumes (such as those near ϕ_{crit}) than more permeable congelation ice. This would support the use of a parameter like ϕ_{crit} to restrict or slow slush layer desalination, since our hybrid desalination method is derived from stable salinity measurements from congelation ice [Nakawo and Sinha, 1981].

[81] The combination of sea ice permeability and brine density gradient are considered primary determinants of desalination rate [Cox and Weeks, 1975; Notz and Worster, 2009]. Measured Arctic sea ice permeabilities span >2.5 orders of magnitude over brine fractions between 0.05 and 0.25, with smaller brine fractions corresponding to lower permeabilities [Golden *et al.*, 2007]. Interestingly, the rate of change in permeability for $\phi > 0.2$ appears to slow, indicating that our critical brine fraction $\phi_{crit} = 0.2$ may correspond with an inflection in the permeability-porosity relationship and may therefore be more generally applicable to situations besides those tested here.

[82] Below $\phi = \sim 0.2$, Golden *et al.* [2007] show that predicted permeability decreases as a continuous function, whereas in our model, the desalination method switches abruptly once an ice layer reaches ϕ_{crit} . Therefore, our model has the potential to accumulate errors in bulk salinity, nutrients or other state variables depending upon the desalination scheme if the sea ice environment lingers at, or repeatedly transits, the ϕ_{crit} boundary. A more continuous transition between the two methods of desalination would help to mitigate such an error. However, further refinement of the desalination method is not warranted without more detailed time series observations against which to test it.

[83] Slush ice may form in situations other than observed at ISW, most notably during initial ice formation as frazil ice consolidates [Wadhams *et al.*, 1987; Lange *et al.*, 1989; Ackley and Sullivan, 1994] and during ice melt [Fritsen *et al.*, 2001; Haas *et al.*, 2001; Ackley *et al.*, 2008]. Given different environmental forcing, our model is able to produce a diverse set of salinity profiles starting from a uniform layer of slush ice representing consolidated frazil ice. Modeled salinity profiles resemble typical observations, including high salinity near the ice surface in new ice, and the C-shape profile common to first year ice (B. T. Saenz, unpublished data, 2011). These results are not shown for the sake of brevity, and because during new ice growth, desalination using the SLDM is effectively similar to the previous models from which it is derived [CW88; Eicken, 1992; Maksym and Jeffries, 2000; Vancoppenolle *et al.*, 2009].

[84] Under conditions of ice warming and melt, sea ice desalination is not expected due to the relaxation or reversal of the vertical brine density gradient, and the SLDM is not

active. We note that the SLDM generally causes more rapid slush desalination than CW88, and the resultant difference in bulk salinity between the two methods will affect subsequent biophysical evolution of the ice pack. Using our model, lower bulk salinities reduce the potential for future thermal generation of gap layers [Ackley *et al.*, 2008] and for brine convection events during melt-freeze cycles compared to models that employ CW88 brine drainage in slush layers [Maksym and Jeffries, 2000].

[85] Sturm *et al.* [1998] observed cold slush layers with dense brine near the surface of Antarctic pack ice during winter. These cold slush layers must arise through concentration of cold brine from the ice matrix, either through upward percolation or by cooling of a warmer slush layer without significant desalination. Under winter conditions, the brine may be 20°C colder than the seawater, and the replacement of cold brine with relatively warm seawater might have non-negligible effects on ice thermodynamics. Evidence of heat transfer by brine convection is implicit in observations of ice stalactites, where cold brine draining from the ice causes new ice growth immediately below brine tubes. In such cases, the SLDM may be inaccurate since the method is based upon observations of desalination near the ice-seawater interface, which remains close to seawater temperature. A more thorough treatment of cold slush layers is currently precluded by a lack of observations.

5.4. Simulation of Sea Ice Algal Growth

[86] In general, our simulations of ISW sea ice algal production and associated tracers closely matched observations, with the exception of nitrate+nitrite measurements following slush layer freeze up. The general pattern in both ISW simulations was exponential algal growth from the start of the simulation until shortly after the freezing front passed through the slush layer. In our simulations, propagation of the freezing front through the slush layer caused the accumulated biomass to quickly exhaust available nitrate, and Chl *a* ceased to increase after day 78 and 80 at ISWB and ISWA, respectively. Limitation by N seems unlikely at ISW, however, since nitrate+nitrite concentrations in the brine remained relatively high in measured ice cores [Fritsen *et al.*, 1994; Ackley *et al.*, 1996]. In the model, as in the observations, other factors that can potentially limit algal growth (irradiance, temperature, and salinity) were still conducive for growth for some time after passage of the freezing front. Therefore, it is not clear what caused the cessation of biomass accumulation at ISW in the presence of high N concentrations. It is possible that another nutrient, such as silicic acid, may have been limiting growth at ISW. Silicic acid does not become limiting before nitrate in our model runs because the seawater is assumed to contain excess silicic acid compared to nitrate, based on the biochemical N:Si requirements of diatoms, the dominant sea ice alga.

[87] One interesting feature of the algal bloom at both ISWB and ISWA, as well as in our simulations, was that maximum algal concentrations were found in a layer of granular ice below the original slush layer [Ackley *et al.*, 1996, Figure 9]. At ISW, introduction of nutrients to this layer during brine convection is likely, given its proximity to the desalinating slush. In addition, the porosity of this region may have increased as new brine channels were created or

enlarged during desalination, thereby creating new habitat for algal colonization. Algae may have migrated downward from the slush layer as well [Welch and Bergmann, 1989]. During simulations, high algal growth in this granular region was promoted by nutrient-rich brine that was mixed in from the adjacent slush layer by the SLDM. Since this region froze later than the slush layer, conditions for algal growth remained optimal for longer than in the slush layer itself and allowed greater algal biomass accumulation. We note that algal migration was not necessary to reproduce high algal biomass in the simulated granular layer; the parameterization of algal migration in the model is dependent upon the positive bottom ice growth rate, and was not active during ISW simulations.

[88] Our simulations show significant increases in total ice column algal biomass through incorporation of water column algae into sea ice brine during bottom freezing (congelation ice growth). The water column algal concentration used here (1 mg Chl *a* m⁻³) is higher than observed values under thick, winter sea ice, but is lower than observations during the algal growth season [Fritsen *et al.*, 2008]. Concentration of water column material within sea ice during ice formation (consolidation of frazil ice) is commonly observed [Garrison *et al.*, 1983; Ackley and Sullivan, 1994; Fritsen *et al.*, 2008], but incorporation of water column algae during congelation ice growth or snow ice formation has not been quantified. Higher or lower rates of algal incorporation during congelation ice growth would change the sea ice algal biomass and the potential for algal production near the bottom of the ice.

[89] Examination of ice algal production has traditionally focused on surface and bottom communities where high algal concentrations are frequently observed, although the ice interior often contains significant algal communities as well [Garrison and Buck, 1989; Arrigo *et al.*, 2010]. These interior communities, while frequently less dense than in slush layers or at the ice bottom, have the potential to contribute a large percentage of total production due to the relatively large volume of ice that they occupy. During our simulations, a large percentage of algal production came from algae that were not concentrated in a particular layer (Figure 9). These blooms resulted from nutrient-replete conditions and warm temperatures present at the start of every simulation. An analogous situation exists during early spring when nutrient concentrations are adequate for an interior ice column bloom in first-year pack ice. These nutrients may either be frozen into the ice during winter or result from remineralization of ice bound organic material [Arrigo and Thomas, 2004]. A full discussion of the relative importance of different algal layers is beyond the scope of the present, although the ability of our model to simulate these different communities using a physics-based approach will allow further examination of this issue.

[90] Through use of the hybrid desalination method and coupled biochemical model components, our model is suited to further investigate the extent and magnitude of convection-fueled interior ice algal blooms. Assumptions inherent in our treatment of modeled brine advection may contribute to errors in algal production, however. Estimates of brine flux volumes at ISW were derived using physical and biological principles rather than directly observed, and span a large range (0.15–1.8 m³ [Fritsen *et al.*, 1994;

Ackley *et al.*, 1996]). Brine flux volumes calculated by dilution in the SLDM fall within this range for the ISW model runs presented here, but this parameterization may not be representative of alternative slush layer configurations and ice conditions. We note that at ISW, the potential nutrient supply calculated using a salt-balance approach exceeded algal demand by 2.7–3 times [Ackley *et al.*, 1996]; for algal concentrations less than or equal to those at ISW, simulations of algal growth in slush may not be sensitive to such high brine fluxes. We know of no subsequent biophysical observations of slush ice, comparable in scope to ISW, which might permit refinement of predicted brine flux volumes.

[91] By assuming that seawater remains constitutionally intact as it advects into desalinating layers via the SLDM, the model ignores potentially significant algal production in large brine channels below. These channels may be up to 0.03 m in diameter [Fritsen *et al.*, 1994] and likely provide a high-quality ice algal habitat with better access to both surface light and seawater nutrients than the surrounding interior ice. For vigorous convection in large brine tubes, the effective-diffusivity desalination treatment of *Vancoppenolle et al.* [2010] may better represent the salinity evolution below slush layers, as it allows bulk salinities to increase and move tracers through every ice layer. Diffusive advection may not accurately describe the rapid, direct convection through large brine channels, however, and as a result, may lead to underestimation of nutrient delivery and algal production in desalinating slush. Uncertainty concerning the magnitude and pathways of brine flux and how it impacts sea ice algal production highlight the need for further time series investigations of sea ice slush layers.

5.5. Application to Large-Scale Simulations

[92] In a fully mechanistic model, the desalination rate of a slush layer would be determined by the balance of convective heating from the seawater below and atmospheric cooling from above, in combination with consideration of the fluid pathway. *Maksym and Jeffries* [2001] use such an approach and similar models are being developed. For example, *Petrich et al.* [2006] employ a hybrid fluid transport model that can simulate brine movement related to gravity drainage in highly porous sea ice using predicted permeabilities. Unfortunately, the two-dimensional nature of such simulations does not lend itself to large-scale investigations. However, patterns of slush layer dynamics and brine flux magnitudes derived from such mechanistic modeling could be adapted and parameterized into models developed for large-scale applications, as we have done here using empirical estimates of sea ice desalination.

[93] *Notz and Worster* [2009] correctly point out that desalination in sea ice is a continuous process across a region of porous sea ice. Indeed salt does not segregate immediately from freezing sea ice to arrive at stable salinity as is implied in our calculations of dS/dt . For the purposes of large-scale simulation, however, the concept of a two-stage desalination process is useful as an aggregator of micro-scale physics over space and time. We have shown that as long as the surface or interior slush layer is resolved by the vertical model structure, our model can correctly simulate the halothermal evolution of the slush-containing ice pack. When applied to a large-scale sea ice simulation, the sea ice

desalination model presented here has the ability to improve estimates of heat and salt fluxes in coupled climate models. The slush layers simulated by our model incorporate the processes required to simulate the magnitude and duration of the algal blooms common to such environments, which are thought to be responsible for the majority of carbon fixation in Antarctic sea ice [Garrison and Buck, 1991; Legendre *et al.*, 1992]. Our future work will involve applying the slush layer dynamics presented here to a hemispheric sea ice model, with the goal of examining pan-Antarctic sea ice algal production over time.

[94] **Acknowledgments.** This work was made possible through a NASA Earth System Science (ESS) Fellowship to Benjamin Saenz, and NASA OES grant NR-A04-OSE-02 to Kevin Arrigo, with assistance from the Stanford School of Earth Sciences. Gert van Dijken provided invaluable scientific, technical, and programming advice. Special thanks to Steve Ackley, Don Perovich, Chris Fritsen, Ken Golden, and Ted Maksym for providing data, helpful advice, comments, and reviews.

References

- Ackley, S., and C. Sullivan (1994), Physical controls on the development and characteristics of Antarctic sea ice biological communities—A review and synthesis, *Deep Sea Res., Part 1*, *41*, 1583–1604, doi:10.1016/0967-0637(94)90062-0.
- Ackley, S., C. Fritsen, V. I. Lytle, and C. W. Sullivan (1996), Freezing driven upwelling in Antarctic sea ice biological systems, *Proc. 17th NIPR Symp. Polar Biol.*, *9*, 45–59.
- Ackley, S. F., M. J. Lewis, C. H. Fritsen, and H. Xie (2008), Internal melting in Antarctic sea ice: Development of “gap layers”, *Geophys. Res. Lett.*, *35*, L11503, doi:10.1029/2008GL033644.
- Andreas, E. L., R. E. Jordan, and A. P. Makshtas (2005), Parameterizing turbulent exchange over sea ice: the ice station Weddell results, *Boundary Layer Meteorol.*, *114*, 439–460, doi:10.1007/s10546-004-1414-7.
- Arrigo, K. R., and C. W. Sullivan (1994), A high-resolution bio-optical model of microalgal growth: testing using sea-ice algal community time-series data, *Limnol. Oceanogr.*, *39*(3), 609–631.
- Arrigo, K. R., and D. N. Thomas (2004), Large scale importance of sea ice biology in the Southern Ocean, *Antarct. Sci.*, *16*(4), 471–486, doi:10.1017/S0954102004002263.
- Arrigo, K. R., J. N. Kremer, and C. W. Sullivan (1993), A simulated Antarctic fast ice ecosystem, *J. Geophys. Res.*, *98*(C4), 6929–6946.
- Arrigo, K., D. Worthen, M. Lizotte, and P. Dixon (1997), Primary production in Antarctic sea ice, *Science*, *276*, 394–397.
- Arrigo, K. R., D. L. Worthen, P. Dixon, and M. P. Lizotte (1998), Primary productivity of near surface communities within Antarctic pack ice, *Antarct. Res. Ser.*, *73*, 23–43.
- Arrigo, K., T. Mock, and M. P. Lizotte (2010), Primary production in sea ice, in *Sea Ice*, 2nd ed., edited by D. N. Thomas and G. S. Dieckmann, pp. 283–325, Wiley-Blackwell, Hoboken, N. J.
- Babin, M., A. Morel, V. Fournier-Sicre, F. Fell, and D. Stramski (2003), Light scattering properties of marine particles in coastal and open ocean waters as related to the particle mass concentration, *Limnol. Oceanogr.*, *48*(2), 843–859.
- Barber, D., R. De Abreu, and E. LeDrew (1991), Optical extinction and microwave scattering within a seasonally varying snow covered sea ice surface, *Geosci. Remote Sens. Symp.*, *2*, 799–802.
- Bissinger, J., D. Montagnes, J. Sharples, and D. Atkinson (2008), Predicting marine phytoplankton maximum growth rates from temperature: Improving on the Eppley curve using quantile regression, *Limnol. Oceanogr.*, *53*(2), 487–493.
- Bitz, C., and W. Lipscomb (1999), An energy-conserving thermodynamic model of sea ice, *J. Geophys. Res.*, *104*(C7), 15,669–15,677.
- Briegleb, B. P., and B. Light (2007), A Delta-Eddington multiple scattering parameterization for solar radiation in the sea ice component of the Community Climate System Model, *NCAR Tech. Note NCAR/TN-472+STR*, pp. 1–108, Natl. Cent. for Atmos. Res., Boulder, Colo.
- Cox, G., and W. Weeks (1975), Brine drainage and initial salt entrapment in sodium chloride ice, report, Cold Reg. Res. and Eng. Lab., Hanover, N. H.
- Cox, G., and W. Weeks (1988), Numerical simulations of the profile properties of undeformed first-year sea ice during the growth season, *J. Geophys. Res.*, *93*(C10), 12,449–12,460.

- Ebert, E., and J. Curry (1993), An intermediate one-dimensional thermodynamic sea ice model for investigating ice-atmosphere interactions, *J. Geophys. Res.*, *98*(C6), 10,085–10,109.
- Ehn, J. K., T. N. Papakyriakou, and D. G. Barber (2008), Inference of optical properties from radiation profiles within melting landfast sea ice, *J. Geophys. Res.*, *113*, C09024, doi:10.1029/2007JC004656.
- Eicken, H. (1992), Salinity profiles of Antarctic sea ice: field data and model results, *J. Geophys. Res.*, *97*(C10), 15,545–15,557.
- Eicken, H., H. R. Krouse, D. Kadko, and D. K. Perovich (2002), Tracer studies of pathways and rates of meltwater transport through Arctic summer sea ice, *J. Geophys. Res.*, *107*(C10), 8046, doi:10.1029/2000JC000583.
- Flato, G., and W. Hibler III (1995), Ridging and strength in modeling the thickness distribution of Arctic sea ice, *J. Geophys. Res.*, *100*(C9), 18,611.
- Freitag, J. (1999), Untersuchungen zur Hydrologie des arktischen Meereseises - Konsequenzen für den kleinskaligen Stofftransport (in German), *Ber. Polarforsch.* *325*, Alfred-Wegener Inst. für Polar- und Meeresforsch., Bremerhaven, Germany.
- Freitag, J., and H. Eicken (2003), Meltwater circulation and permeability of Arctic summer sea ice derived from hydrological field experiments, *J. Glaciol.*, *49*, 349.
- Fritsen, C. H., V. Lytle, S. F. Ackley, and C. Sullivan (1994), Autumn bloom of Antarctic pack-ice algae, *Science*, *266*, 264–266.
- Fritsen, C. H., S. F. Ackley, J. N. Kremer, and C. W. Sullivan (1998), Flood-freeze cycles and microalgal dynamics in Antarctic pack ice, in *Antarctic Sea Ice: Biological Processes, Interactions and Variability*, *Antarct. Res. Ser.*, vol. 73, edited by M. P. Lizotte and K. R. Arrigo, pp. 1–22, AGU, Washington, D. C.
- Fritsen, C. H., S. L. Coale, D. R. Neenan, A. H. Gibson, and D. L. Garrison (2001), Biomass, production and microhabitat characteristics near the freeboard of ice floes in the Ross Sea, Antarctica, during the austral summer, *Ann. Glaciol.*, *33*, 280–286.
- Fritsen, C. H., J. Memmott, and F. Stewart (2008), Inter-annual sea-ice dynamics and micro-algal biomass in winter pack ice of Marguerite Bay, Antarctica, *Deep Sea Res., Part II*, *55*(18–19), 2059–2067, doi:10.1016/j.dsr2.2008.04.034.
- Fukasako, S. (1990), Thermophysical properties of ice, snow, and sea ice, *Int. J. Thermophys.*, *11*(2), 353–372.
- Garrison, D., and K. Buck (1989), The biota of Antarctic pack ice in the Weddell Sea and Antarctic Peninsula regions, *Polar Biol.*, *10*(3), 211–219.
- Garrison, D., and K. Buck (1991), Surface-layer sea ice assemblages in Antarctic pack ice during the austral spring: Environmental conditions, primary production and community structure, *Oldendorf*, *75*(2), 161–172.
- Garrison, D. L., S. F. Ackley, and K. R. Buck (1983), A physical mechanism for establishing algal populations in frazil ice, *Nature*, *306*, 363–365.
- Golden, K. M., S. F. Ackley, and V. I. Lytle (1998), The percolation phase transition in sea ice, *Science*, *282*, 2238–2241.
- Golden, K. M., H. Eicken, A. L. Heaton, J. Miner, D. J. Pringle, and J. Zhu (2007), Thermal evolution of permeability and microstructure in sea ice, *Geophys. Res. Lett.*, *34*, L16501, doi:10.1029/2007GL030447.
- Gregg, W., and K. Carder (1990), A simple spectral solar irradiance model for cloudless maritime atmospheres, *Limnol. Oceanogr.*, *35*(8), 1657–1675.
- Grenfell, T. C., and G. A. Maykut (1977), The optical properties of ice and snow in the Arctic Basin, *J. Glaciol.*, *18*, 445–463.
- Haas, C., D. N. Thomas, and J. Bareiss (2001), Surface properties and processes of perennial Antarctic sea ice in summer, *J. Glaciol.*, *47*, 613–625.
- Holland, M. M., M. C. Serreze, and J. Stroeve (2008), The sea ice mass budget of the Arctic and its future change as simulated by coupled climate models, *Clim. Dyn.*, *34*(2–3), 185–200, doi:10.1007/s00382-008-0493-4.
- Hudier, E., R. Ingram, and K. Shirasawa (1995), Upward flushing of sea water through first year ice, *Atmos. Ocean*, *33*(3), 569–580.
- Hunke, E., and J. Dukowicz (1997), An elastic-viscous-plastic model for sea ice dynamics, *J. Phys. Oceanogr.*, *27*, 1849–1867.
- Jackson, M., and M. Cheadle (1998), A continuum model for the transport of heat, mass and momentum in a deformable, multicomponent melt, undergoing solid-liquid phase change, *Int. J. Heat Mass Transfer*, *41*(8–9), 1035–1048.
- Jin, Z., K. Stamnes, W. F. Weeks, and S. Tsay (1994), The effect of sea ice on the solar energy budget in the atmosphere-sea ice-ocean system: A model study, *J. Geophys. Res.*, *99*(C12), 25,281–25,294, doi:10.1029/94JC02426.
- Kattner, G., D. Thomas, C. Haas, H. Kennedy, and G. Dieckmann (2004), Surface ice and gap layers in Antarctic sea ice: highly productive habitats, *Mar. Ecol. Prog. Ser.*, *277*, 1–12.
- Kottmeier, C., K. Frey, M. Hasel, and O. Eisen (2003), Sea ice growth in the eastern Weddell Sea in winter, *J. Geophys. Res.*, *108*(C4), 3125, doi:10.1029/2001JC001087.
- Lange, M. A., S. F. Ackley, P. Wadhams, G. S. Dieckmann, and H. Eicken (1989), Development of sea ice in the Weddell Sea, Antarctica, *Ann. Glaciol.*, *12*, 92–96.
- Lavoie, D., K. Denman, and C. Michel (2005), Modeling ice algal growth and decline in a seasonally ice-covered region of the Arctic (Resolute Passage, Canadian Archipelago), *J. Geophys. Res.*, *110*, C11009, doi:10.1029/2005JC002922.
- Legendre, L., S. Ackley, G. Dieckmann, B. Gulliksen, R. Horner, T. Hoshiai, I. Melnikov, W. Reebergh, M. Spindler, and C. Sullivan (1992), Ecology of sea ice biota, *Polar Biol.*, *12*, 429–444.
- Light, B., G. Maykut, and T. C. Grenfell (2003), A two-dimensional Monte Carlo model of radiative transfer in sea ice, *J. Geophys. Res.*, *108*(C7), 3219, doi:10.1029/2002JC001513.
- Light, B., G. A. Maykut, and T. C. Grenfell (2004), A temperature-dependent, structural-optical model of first-year sea ice, *J. Geophys. Res.*, *109*, C06013, doi:10.1029/2003JC002164.
- Light, B., T. C. Grenfell, and D. K. Perovich (2008), Transmission and absorption of solar radiation by Arctic sea ice during the melt season, *J. Geophys. Res.*, *113*, C03023, doi:10.1029/2006JC003977.
- Lipscomb, W., and E. Hunke (2004), Modeling sea ice transport using incremental remapping, *Mon. Weather Rev.*, *132*(6), 1341–1354.
- Lytle, V., and S. F. Ackley (1996), Heat flux through sea ice in the western Weddell Sea: Convective and conductive transfer processes, *J. Geophys. Res.*, *101*(C4), 8853–8868.
- Maksym, T., and M. O. Jeffries (2000), A one-dimensional percolation model of flooding and snow ice formation on Antarctic sea ice, *J. Geophys. Res.*, *105*(C11), 26,313–26,331.
- Maksym, T., and M. O. Jeffries (2001), Phase and compositional evolution of the flooded layer during snow-ice formation on Antarctic sea ice, *Ann. Glaciol.*, *33*, 37.
- Maykut, G. A., and N. Untersteiner (1971), Some results from a time-dependent thermodynamic model of sea ice, *J. Geophys. Res.*, *76*(4), 1550–1576.
- McClain, C. R., K. Arrigo, K. Tai, and D. Turk (1996), Observations and simulations of physical and biological processes at ocean weather station P, 1951–1980, *J. Geophys. Res.*, *101*, 3697–3713, doi:10.1029/95JC03052.
- Melnikov, I. (1998), Winter production of sea ice algae in the western Weddell Sea, *J. Mar. Syst.*, *17*(1–4), 195–205.
- Nakawo, M., and N. Sinha (1981), Growth rate and salinity profile of first-year sea ice in the high Arctic, *J. Glaciol.*, *27*(96), 315–330.
- Niedrauer, T. M., and S. Martin (1979), An experimental study of brine drainage and convection in young sea ice, *J. Geophys. Res.*, *84*(C3), 1176–1186.
- Notz, D., and M. G. Worster (2009), Desalination processes of sea ice revisited, *J. Geophys. Res.*, *114*, C05006, doi:10.1029/2008JC004885.
- Petrich, C., P. J. Langhorne, and Z. F. Sun (2006), Modelling the interrelationships between permeability, effective porosity and total porosity in sea ice, *Cold Reg. Sci. Technol.*, *44*(2), 131–144, doi:10.1016/j.coldregions.2005.10.001.
- Pringle, D., H. Eicken, H. Trodahl, and L. Backstrom (2007), Thermal conductivity of landfast Antarctic and Arctic sea ice, *J. Geophys. Res.*, *112*, C04017, doi:10.1029/2006JC003641.
- Schulze, T. P., and M. G. Worster (1999), Weak convection, liquid inclusions and the formation of chimneys in mushy layers, *J. Fluid Mech.*, *388*, 197.
- Sicko-Goad, L. M., C. L. Schelske, and E. F. Stoermer (1984), Estimation of intracellular carbon and silica content of diatoms from natural assemblages using morphometric techniques, *Limnol. Oceanogr.*, *29*(6), 1170–1178.
- Sturm, M., and R. A. Massom (2009), Snow and sea ice, in *Sea Ice*, 2nd ed., edited by D. N. Thomas and G. S. Dieckmann, pp. 153–204, Wiley-Blackwell, Hoboken, N. J.
- Sturm, M., K. Morris, and R. Massom (1998), The winter snow cover of the West Antarctic pack ice: Its spatial and temporal variability, in *Antarctic Sea Ice: Physical Processes, Interactions and Variability*, *Antarct. Res. Ser.*, vol. 74, edited by M. O. Jeffries, pp. 19–40, AGU, Washington, D. C.
- Sturm, M., D. Perovich, and J. Holmgren (2002), Thermal conductivity and heat transfer through the snow on the ice of the Beaufort Sea, *J. Geophys. Res.*, *107*(C10), 8043, doi:10.1029/2000JC000409.
- Tannehill, J. C., D. A. Anderson, and R. H. Pletcher (1997), *Computational Fluid Mechanics and Heat Transfer*, 2nd ed., 792 pp., Taylor and Francis, Philadelphia, Pa.
- Vancoppenolle, M., T. Fichefet, H. Goosse, S. Bouillon, G. Madec, and M. A. M. Maqueda (2009), Simulating the mass balance and salinity of

- Arctic and Antarctic sea ice. 1. Model description and validation, *Ocean Modell.*, 27(1–2), 33–53, doi:10.1016/j.ocemod.2008.10.005.
- Vancoppenolle, M., H. Goosse, A. De Montety, T. Fichefet, B. Tremblay, and J.-L. Tison (2010), Modeling brine and nutrient dynamics in Antarctic sea ice: The case of dissolved silica, *J. Geophys. Res.*, 115, C02005, doi:10.1029/2009JC005369.
- Wadhams, P., M. A. Lange, and S. F. Ackley (1987), The ice thickness distribution across the Atlantic sector of the Antarctic Ocean in midwinter, *J. Geophys. Res.*, 92(C13), 14,535–14,552, doi:10.1029/JC092iC13p14535.
- Wakatsuchi, M., and N. Ono (1983), Measurements of salinity and volume of brine excluded from sea ice, *J. Geophys. Res.*, 88(C5), 2943–2951.
- Warren, S. (1982), Optical properties of snow, *Rev. Geophys.*, 20(1), 67–89.
- Warren, S., and W. Wiscombe (1980), A model for the spectral albedo of snow. II: Snow containing atmospheric aerosols, *J. Atmos. Sci.*, 37(12), 2734–2745.
- Welch, H., and M. Bergmann (1989), Seasonal development of ice algae and its prediction from environmental factors near Resolute, NWT, Canada, *Can. J. Fish. Aquat. Sci.*, 46(10), 1793–1804.
- Wettlaufer, J. S., M. G. Worster, and H. E. Huppert (1997), The phase evolution of young sea ice, *Geophys. Res. Lett.*, 24, 1251–1254, doi:10.1029/97GL00877.
- Worster, M. G. (1997), Natural convection in a mushy layer, *J. Fluid Mech.*, 224, 335–359.
- Wu, X., W. F. Budd, V. I. Lytle, and R. A. Massom (1999), The effect of snow on Antarctic sea ice simulations in a coupled atmosphere-sea ice model, *Clim. Dyn.*, 15, 127, doi:10.1007/s003820050272.
- Zhang, J., and D. Rothrock (2003), Modeling global sea ice with a thickness and enthalpy distribution model in generalized curvilinear coordinates, *Mon. Weather Rev.*, 131(5), 845–861.

K. R. Arrigo and B. T. Saenz, Department of Environmental Earth System Science, Stanford University, 473 Via Ortega, Stanford, CA 94708, USA. (blsaenz@gmail.com)